

From the Department of Molecular Medicine and Surgery,  
Section for Radiology, Karolinska University Hospital and  
Karolinska Institute, Stockholm, Sweden.

# NERVE DIFFUSION TENSOR IMAGING

Mikael Skorpil  
M.D.



**Karolinska  
Institutet**

Stockholm 2012

All previously published papers were reproduced with permission from the publisher.

Published by Karolinska Institutet. Printed by Larserics Digital Print AB.

© Mikael Skorpil, 2012  
ISBN 978-91-7457-904-8

# ABSTRACT

Diffusion tensor imaging (DTI) is a magnetic resonance imaging technique that *in vivo* visualises random translational movement of water molecules. DTI has inherent difficulties with low signal-to-noise ratio, sensitivity to patient motion, field inhomogeneities and fast T2 relaxation. It has been used in the central nervous system, although it has not been assessed in the peripheral nervous system. The aim of this thesis was to investigate if DTI in peripheral nerves was feasible, and if so, to investigate clinical implications.

Study I showed that in healthy volunteers the peripheral nerves, the sciatic nerves, could be visualised *in vivo* using DTI and fiber tracking. Study II showed that sciatic nerves, including their division into the tibial and common fibular nerves, have a characteristic diffusion pattern with most impaired diffusion perpendicular to the nerve direction. This allowed nerves, excluding other tissues and artifacts, to be visualised using a novel approach called diffusion-direction-dependent imaging and with a simple unidirectional diffusion maximum-intensity projection approach. Study III showed that the olfactory bulbs (OBs) and olfactory tracts could be visualised *in vivo* using DTI and fiber tracking. In Study IV, Parkinson's disease (PD) patients with impaired olfaction were evaluated with DTI of the OBs. A novel approach of DTI was used, taking advantage of the technique's inherent directional information, for region of interest placement and diffusion measurements in the OBs. In the PD patient group diffusion was altered in the OBs, compared to healthy controls. This was hypothesised, since  $\alpha$ -synuclein inclusions and Lewy neurites interfering with nerve structure have been detected in the OBs. However, the coefficient of variation between two identical DTI series was high, due to the small size of the OBs and their location in an area susceptible to artifacts, and the difference between the groups was statistically significant only for the first of two series. In Study V, patients of the Swedish 'Huddinge Spinocerebellar ataxia (SCA) Family' with peripheral neuropathy, were evaluated with DTI of a peripheral nerve. Diffusion alterations were found in peripheral nerves in SCA patients, compared to healthy controls, which was statistically significant.

In conclusion, DTI in peripheral nerves is feasible and can be used to detect diffusion alterations in OBs in PD patients and in peripheral nerves in SCA patients with peripheral neuropathy.



# LIST OF PUBLICATIONS

This thesis is based on the following papers, referred to in the text by their Roman numerals:

- I            Mikael Skorpil, Magnus Karlsson, Anders Nordell.  
**Peripheral nerve diffusion tensor imaging.**  
Magn Reson Imaging 2004;22(5):743-5.
- II           Mikael Skorpil, Mathias Engström, Anders Nordell.  
**Diffusion-direction-dependent imaging - a novel MRI approach for peripheral nerve imaging.**  
Magn Reson Imaging 2007 Apr;25(3):406-11.
- III          Mikael Skorpil, Tyler Rolheiser, Harold Robertson, Anders Sundin, Per Svenningsson.  
**Diffusion tensor fiber tractography of the olfactory tract.**  
Magn Reson Imaging 2011 Feb;29(2):289-92.
- IV          Mikael Skorpil, Veli Söderlund, Anders Sundin, Per Svenningsson.  
**MRI Diffusion in Parkinson's Disease: Using the Technique's Inherent Directional Information to Study the Olfactory Bulb and Substantia Nigra.**  
Journal of Parkinson's Disease 2 (2012) 171-180.
- V           Mikael Skorpil, Martin Paucar, Martin Engvall, Roberto Vargas, Per Svenningsson.  
**The 'Huddinge Spinocerebellar Ataxia Family' - MRI analysis of brain, spinal cord and peripheral nerve.**  
Manuscript.

Papers I-III are reprinted with permission from Elsevier Ltd. and paper IV with permission from IOS Press.



# LIST OF ABBREVIATIONS

ADC	Apparent diffusion coefficient
B-value	‘Diffusion-sensitising factor’
CC	Corpus callosum
CNS	Central nervous system
CV	Coefficient of variation
DaTSCAN	<sup>123</sup> I-Ioflupane single-photon emission computed tomography
DDI	Diffusion-direction-dependent imaging
DTI	Diffusion tensor imaging
DWI	Diffusion-weighted imaging
ENeG	Electroneurography
EPI	Echo planar imaging
FA	Fractional anisotropy
FA-CEI	Fractional anisotropy colour encoded images
FOV	Field of view
MIP	Maximum-intensity projection
MRI	Magnetic resonance imaging
MTR	Magnetisation transfer ratio
NSA	Number of signal averages
OB	Olfactory bulb
PD	Parkinson’s disease
PNP	Peripheral neuropathy
PNS	Peripheral nervous system
REM	Rapid eye movement
REST	Regional saturation technique
RF	Radiofrequency
ROI	Region of interest
SARA	Scale for the assessment and rating of ataxia
SCA	Spinocerebellar ataxia
SENSE	Sensitivity encoding
SN	Substantia nigra
SNR	Signal-to-noise ratio
SPAIR	Spectral adiabatic inversion recovery
SPECT	Single-photon emission computed tomography
SPIR	Spectral presaturation with inversion recovery
TR	Repetition time
TE	Echo time
UPSIT	University of Pennsylvania smell identification test





# TABLE OF CONTENTS

<b>1.</b>	<b>AIMS OF THE THESIS</b>	<b>3</b>
<b>2.</b>	<b>INTRODUCTION</b>	<b>5</b>
2.1	NEUROANATOMY	5
2.1.1	Peripheral nerves	5
2.1.2	Olfactory nerves and olfaction	6
2.2	MAGNETIC RESONANCE IMAGING	7
2.2.1	T2 and T1 relaxation	10
2.2.2	MRI images and k-space	11
2.3	DIFFUSION-WEIGHTED IMAGING	12
2.4	DIFFUSION TENSOR IMAGING	14
2.4.1	Nerves and DTI	15
2.4.2	Fractional anisotropy colour encoded images and fiber tracking	16
2.4.3	Compartments	16
2.5	MAGNETIC FIELD	16
2.6	MAGNETISATION TRANSFER IMAGING	17
2.7	PARKINSON'S DISEASE	17
2.7.1	Hyposmia	19
2.8	SPINOCEREBELLAR ATAXIA	19
<b>3.</b>	<b>MATERIAL AND METHODS</b>	<b>21</b>
3.1	HEALTHY INDIVIDUALS AND PATIENTS	21
3.2	MR-SCANNERS	21
3.3	COILS	22
3.4	DIFFUSION-WEIGHTED SEQUENCES	22
3.4.1	Fiber tracking	24
3.4.2	Diffusion-direction-dependent imaging	24
3.4.3	Inherent diffusion directional information	26
3.5	MAGNETISATION TRANSFER SEQUENCE	28
3.6	T1-, T2- AND PROTON DENSITY-WEIGHTED SEQUENCES	29
3.7	OLFACTION TESTING	30
3.8	MRI VOLUMETRY AND SPINAL CORD MEASUREMENTS	30
<b>4.</b>	<b>RESULTS</b>	<b>31</b>
4.1	PERIPHERAL NERVE DIFFUSION TENSOR IMAGING	31
4.2	DIFFUSION-DIRECTION-DEPENDENT PERIPHERAL NERVE IMAGING	31
4.3	DIFFUSION TENSOR FIBER TRACTOGRAPHY OF THE OLFACTORY TRACT	32
4.4	MRI DIFFUSION IN PARKINSON'S DISEASE: USING THE TECHNIQUE'S INHERENT DIRECTIONAL INFORMATION TO STUDY THE OLFACTORY BULB AND SUBSTANTIA NIGRA	32

4.5	THE ‘HUDDINGE SPINOCEREBELLAR ATAXIA FAMILY’ – MRI ANALYSIS OF BRAIN, SPINAL CORD AND PERIPHERAL NERVE	34
4.5.1	Clinical details, ENeG, brain and spinal cord volume alterations	35
<b>5.</b>	<b>DISCUSSION</b>	<b>37</b>
5.1	NERVE DIFFUSION TENSOR IMAGING	37
5.2	CLINICAL IMPLICATIONS	49
5.2.1	Other published studies	49
5.3	NERVE DIFFUSION TENSOR IMAGING CONSIDERATIONS	51
5.3.1	The optimal voxel	55
5.4	PARKINSON’S DISEASE – SUBSTANTIA NIGRA AND CORPUS CALLOSUM	55
5.5	THE ‘HUDDINGE SPINOCEREBELLAR ATAXIA FAMILY’ – BRAIN AND SPINAL CORD	56
<b>6.</b>	<b>CONCLUSIONS</b>	<b>59</b>
<b>7.</b>	<b>REFERENCES</b>	<b>61</b>
<b>8.</b>	<b>ACKNOWLEDGEMENTS</b>	<b>71</b>





# **1. AIMS OF THE THESIS**

The aim of the thesis was to investigate if diffusion tensor imaging (DTI) in peripheral nerves was feasible, and if so, to investigate clinical implications.



## 2. INTRODUCTION

### 2.1 NEUROANATOMY

The central nervous system (CNS) constitutes of the brain and spinal cord, whilst the peripheral nervous system (PNS) is constituted of nerve structures outside the pial membrane of the brainstem and spinal cord. There are 12 pairs of cranial nerves exiting from the brain. The optic nerve (I) and olfactory nerve (II) are brain extension, thus part of the CNS, while the cranial nerves III-XII are part of the PNS<sup>1</sup>. There are 8 pairs of cervical, 12 pairs of thoracic, 5 pairs of lumbar, 5 pairs of sacral and one pair of coccygeal nerves. The brain is further divided into the cerebrum, brainstem and cerebellum, with the brainstem divided into the mesencephalon, pons and medulla oblongata.

#### 2.1.1 Peripheral nerves

A peripheral nerve cell, a neuron, is constituted of a cell body and a long cell projection called axon, both containing organelles and cytoskeleton. Cell bodies of motor neurons are located in the ventral horns of the spinal cord and cell bodies of the sensory neurons in the dorsal spinal ganglions. The axon conducts the electric impulse<sup>2</sup>. Motor and sensory axons are surrounded by a myelin sheath, i.e. axons are myelinated, and the myelin is organised in concentric double phospholipid layers<sup>3</sup>. At small nodes along the axons there is no myelin, and the electric impulse 'jumps' between these nodes, which speeds up nerve conduction. The internodal myelin is supplied and produced by one Schwann cell (in the CNS, myelin is produced by oligodendrocytes). Axons that conduct heat and pain are unmyelinated<sup>1,2,4,5</sup>.

Each axon is surrounded by loose connective tissue called endoneurium. Several axons are bunched together in fascicles, which are surrounded by multiple layers of dense connective tissue called perineurium. These fascicles are themselves bunched together and surrounded by dense irregular connective tissue, with thick collagen and elastin fibers, called epineurium. Proximally the epineurium is continuous with the dural membrane. This connective tissue, which supports and protects the nerves, is produced by fibroblasts. Within the perineurium and epineurium there are many anastomosing capillaries. In larger nerves, variable amounts of interfascicular adipose tissue (loose perineurium) are present. In this thesis, the term *nerve fiber* is used for nerve fibers that are seen for the naked eye, thus several millimeters in diameter. The myelinated axon diameter is approximately 4-10  $\mu\text{m}$ , the myelin itself 0.5-2  $\mu\text{m}$  thick with 0.5-2  $\mu\text{m}$  extraaxonal separation. The myelin sheaths extend, i.e. the internodal distance, approximately 250-1000  $\mu\text{m}$ <sup>1,2,4,5</sup>. The thickness of myelin is proportional to the axon diameter,

which in turn is proportional to the internodal distance<sup>2</sup>. The diameter of a myelinated nerve axon is directly proportional to its conduction velocity<sup>6</sup>. Unmyelinated axons are approximately 0.2-3.0  $\mu\text{m}$  in diameter and more numerous than myelinated axons<sup>1</sup>. Approximately 5-20 unmyelinated axons are bundled together with cytoplasm from one Schwann cell, isolating the axons from each other. If a nerve biopsy is required in patients, it is often performed on the sural nerve. It is an almost purely sensory nerve and the myelinated axons are approximately 2-16  $\mu\text{m}$  in diameter<sup>2</sup>.

In pathological conditions, either the axon/cell body or myelin/Schwann cell is primarily affected, with the counterpart often being affected secondarily. In axonopathy the axon is primarily affected and in neuronopathy the cell body. In axonopathy there is axonal degeneration and secondarily the myelin disintegrates. A focal traumatic lesion leads to Wallerian degeneration of the distal portion of the axon. In slowly evolving axonopathies and neuronopathies only few nerve cells are simultaneously affected. Disease evidence can therefore be sparse on histopathological examination. Secondarily to axonal degeneration, muscles lose their neural input and become atrophic<sup>2</sup>.

Segmental demyelination occurs when the Schwann cell or the myelin sheath is primarily affected. Schwann cells are affected irregularly with an uneven demyelination of the axon. Remyelination can occur, although the myelin sheath will be thinner and the internodal distance shorter. Many chronic demyelinating neuropathies are followed by axonal degeneration<sup>2</sup>.

### **2.1.2 Olfactory nerves and olfaction**

The olfactory bulb (OB) together with the olfactory tract is often called the 'olfactory nerve', although the real olfactory nerves are the numerous bipolar neurons connecting through the cribriform plate. These neurons are the only ones connecting CNS directly with the external environment<sup>1,7</sup>. From the substantia perforata anterior, at the inferior surfaces of the frontal lobes, medial, intermediate and lateral striae exit the brain and unite to form the olfactory tract. The olfactory tract enlarges distally into the OB which is a brain extension. The olfactory tracts are localised in the olfactory sulci and distally, including OBs, in the olfactory grooves of the ethmoidal bone<sup>7</sup>.

Olfactory receptors are located within the mucus of the olfactory epithelium, in the upper and posterior parts of the nasal cavity, just inferior to the cribriform plate. These chemosensitive receptors are dendritic projections from the olfactory cell bodies located in the mucosa<sup>1</sup>. Unmyelinated axons project from these cell bodies through the cribriform plate to the OB, where they in glomeruli synapse with mitral and tufted cells. The OB consists of 6 cellular layers<sup>8</sup> with



afferent and efferent myelinated fibers running in the olfactory tract to the brain. Although a few axons cross the midline through the anterior commissure, olfaction is regarded as an uncrossed sense<sup>1,7</sup>. Located inferior within the OB and olfactory tract are cells of the anterior olfactory nucleus, which are affected early in Parkinson's disease<sup>9</sup>. Olfaction is unique as a sense, in that it is partially directly connected to the cerebral cortex and partially via thalamus. Olfactory central brain areas are the orbitofrontal area, connecting through the thalamus, and the piriform and entorhinal areas connecting directly with the olfactory tracts. Olfaction does not have a central topographic organisation, which by contrast is seen in visual and sensory senses. There are approximately 1000 different olfactory receptor types and approximately 10000 neurons of each receptor type. Glomeruli in OB are connected to neurons expressing the same receptor type<sup>7,10</sup>.

## 2.2 MAGNETIC RESONANCE IMAGING

In 2003 Sir Peter Mansfield and Paul C. Lauterbur were awarded the Noble Prize 'for their discoveries concerning magnetic resonance imaging'. Magnetic resonance imaging (MRI), also called nuclear magnetic resonance imaging, produce images based on properties of atomic nuclei that possess a total non-zero spin. In a simplified view, spin is angular momentum of particles and since atomic nuclei are positively charged, those with a total non-zero spin will behave as small magnets (Figure 1).

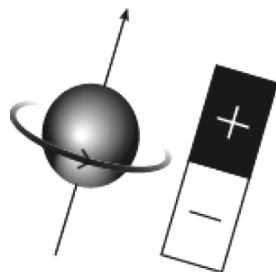
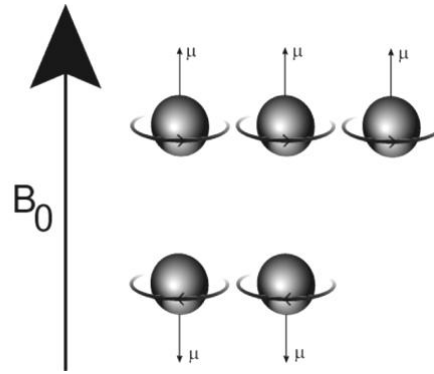


Figure 1. A spinning proton behaves like a magnet.

The hydrogen nucleus constitutes of one proton and hydrogen is abundant in the human body (approximately 63%), mainly as part of water and fat. It is the most common nucleus used for MRI, while phosphor is an example of another nucleus used. MR-scanners use a large external magnetic field,  $B_0$ , to align hydrogen nuclei (and other nuclei with a total non-zero spin) in the same or opposite direction of the magnetic field. Aligned in same direction of the magnetic field is the low-energy state, while in the opposite direction is the high-energy state (there is a dynamic equilibrium between the two states). A higher proportion of the protons is aligned along the magnetic field, although the difference is very small (Figure 2).

Figure 2. A slightly higher proportion of the protons is aligned in the same direction as the magnetic field.



At 1.5 Tesla this proportion (in room temperature) is approximately 1.5 parts per million and at 3.0 Tesla 3 parts per million. Nuclei with a total non-zero spin will precess around the external magnetic field with a unique frequency, called the Larmor frequency,  $\omega_0$ . At 1.5 T it is for hydrogen 63 Mhz (63 million times per second, for comparison it is for phosphor 26 Mhz at 1.5 T) and it is 128 Mhz at 3.0 T. The Larmor frequency is shown in Equation [1].

$$\omega_0 = B_0 \gamma \quad [1]$$

It depends on the external magnetic field  $B_0$  and the gyromagnetic ratio  $\gamma$ , which is specific for atomic nuclei. The small proportion of protons that is aligned along the magnetic field can be viewed as a collective magnetic vector,  $M$ , constituted of the sum of each proton's magnetic vector,  $\mu$  (Figure 3).

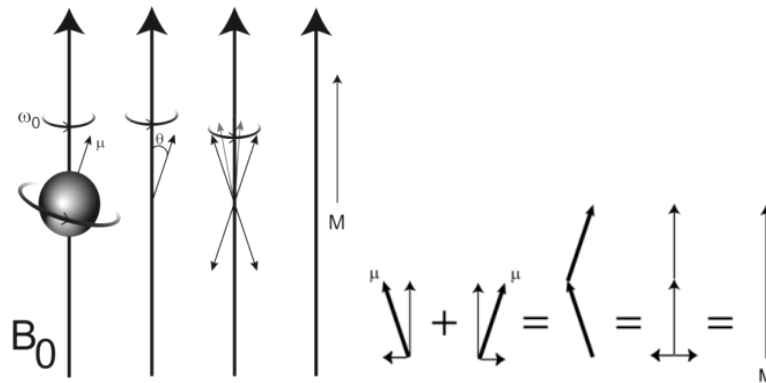


Figure 3. Protons are precessing around  $B_0$  with frequency  $\omega_0$  at an angle  $\theta$ . Each proton's magnetic vector  $\mu$  is summarised to a collective  $M$  vector.

A radiofrequency (RF) pulse is transmitted with a coil (electromagnetic waves/photons). If the transmitted frequency is the same as for the  $\omega_0$ , i.e. the resonance frequency, the protons get excited. The RF pulse is created with an alternating current, likewise an alternating magnetic field,  $B_1$ . This alternating  $B_1$  can be viewed as two magnetic fields rotating in opposite directions (Figure 4).

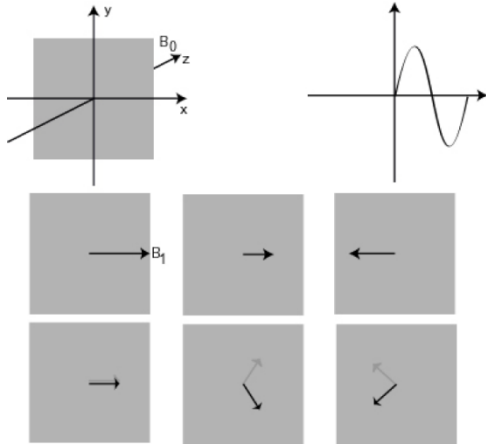
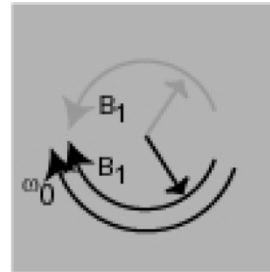


Figure 4.  $B_1$  is an alternating magnetic field (middle row), which also can be viewed as two magnetic fields rotating in opposite directions (lower row).  $B_1$  plane is 90 degrees against  $B_0$  (upper row left) and a sinusoidal curve showing an alternating magnetic field (upper row right).

Since one of the rotating magnetic fields is rotating in the same direction and at the same speed as  $\omega_0$ , energy can be exchanged, i.e. resonance (Figure 5).

Figure 5. One of the  $B_1$  components is rotating in the same direction and frequency as  $\omega_0$ , i.e. resonance.



Since  $B_1$  is a magnetic field,  $M$  will rotate around both  $B_1$  and  $B_0$ . Since  $B_1$  and  $\omega_0$  have the same frequency, this can be seen isolated as a 'rotating frame of reference', i.e.  $M$  is rotating around  $B_1$  (Figure 6).

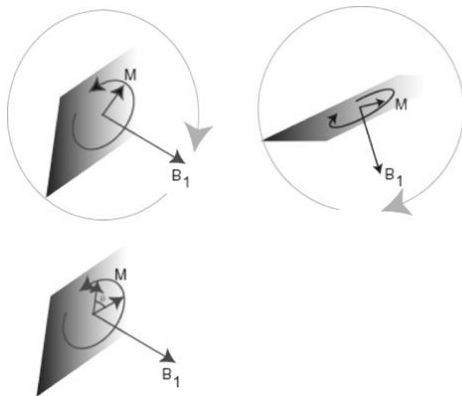
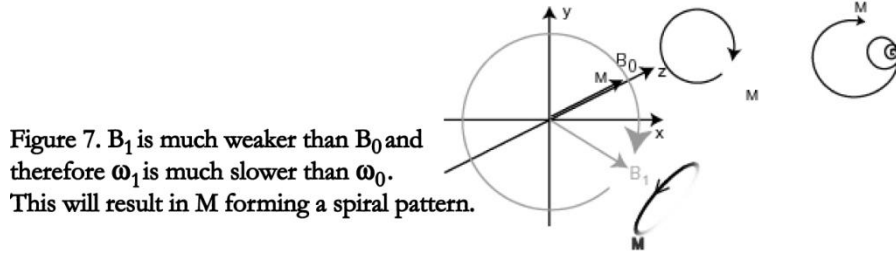


Figure 6. When  $B_1$  is applied  $M$  will start rotating around  $B_1$  (upper row).  $M$  consists of multiple  $\mu$  and will therefore still rotate around  $B_0$ . As  $M$  is rotating at the same frequency as  $B_1$ , this can be viewed isolated as a 'rotating frame of reference', i.e.  $M$  rotating around  $B_1$  (bottom row).

Depending on the strength and length of the RF pulse,  $M$  will 'flip', i.e. rotate, a specific angle around  $B_1$ , e.g. 90 degrees. When not seen in the 'rotating frame of reference', according to Eq. [1], since  $B_1 \ll B_0$  then  $\omega_1 \ll \omega_0$ ,  $M$  will form a spiral pattern (Figure 7).



When the RF pulse is turned off, the protons will return to their equilibrium, thus relax and emit RF waves, which are received by a coil and used to produce images. The time to reach equilibrium depends on exponential T1 and T2 relaxation times.

### 2.2.1 T2 and T1 relaxation

Relaxation of magnetisation in the transverse direction  $M_{xy}$  constitutes the T2 relaxation time

$$M_{xy} = \frac{M_{xy0}}{e^{t/T_2}} = M_{xy0} e^{-t/T_2} \quad [2]$$

and relaxation in the longitudinal direction  $M_z$  the T1 relaxation time.

$$M_z = M_{z0} (1 - e^{-t/T_1}) \quad [3]$$

T2 relaxation is ‘spin-spin relaxation’. There are always fluctuations/motion in materia, even at zero Kelvin degrees (otherwise the Heisenberg uncertainty principle would be incorrect). As a consequence, protons will come closer or farther away from other protons, and the local magnetic field will thereby increase or decrease. According to Eq. [1] the frequency will increase or decrease and the protons will dephase, thus the spins will precess less coherently (Figure 8).

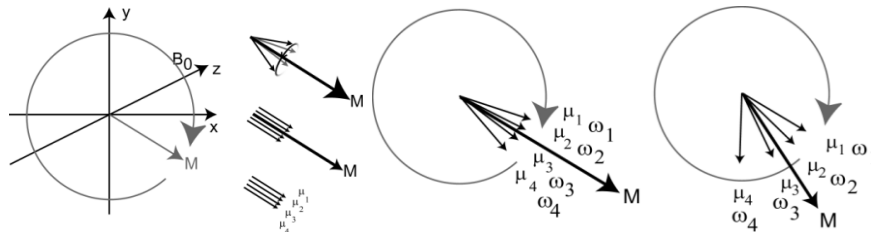


Figure 8.  $M$  consists of numerous  $\mu$ . If protons are subjected to slightly different  $B_0$  they will no longer precess coherently. The protons dephase and  $M$  exponentially decreases.

T2 relaxation is a non-reversible process and it is shorter for lipids than for water. Larger molecules, such as lipids, as compared to water, comprise more protons and

have a larger local magnetic field. These larger molecules also have slower motion than smaller molecules. This will result in larger variations in the local magnetic field, since larger molecules can remain in contact for a longer period. In solids, T2 relaxation is very short, since the local magnetic field variation is fixed, while liquids having motion of material lessen the effect. Inhomogeneities in  $B_0$  will also contribute to T2 relaxation. This can be reversed in a spin echo sequence, but not in a gradient echo sequences. In gradient echo sequences the relaxation time is therefore denoted  $T2^*$ .

Longitudinal relaxation, called ‘spin-lattice relaxation’, is T1 relaxation. During this process energy is returned to the lattice, i.e. the tissue. This can occur when fluctuations in tissues are similar to the  $\omega_0$  and will depend on several factors. Two of them are molecule size and the presence of macromolecules. Very large molecules have slow motion impeding this process, while for small molecules, e.g. water, the motion is too fast. Medium-sized molecules have the best energy transfer and T1 relaxation is consequently shorter for fat than for water. Macromolecules, e.g. proteins, with available hydrophilic binding sites will also shorten T1. Water will form hydration layers, both at the binding sites and unbound water close to the molecules. This will slow down water motion and make energy transfer easier.

## 2.2.2 MRI images and k-space

Conventional MRI images are constructed of pixels with signal intensity (S) depending on the registered amplitude of the voxel’s magnetic vector  $M_{xy}$ . The signal intensity measures will depend on many parameters, e.g. tissue relaxation time, number of protons, repetition time (TR), echo time (TE), other pulse sequence parameters, magnetic field, coil, matrix and slice thickness.

Since the vector  $M_{xy}$  is rotating, it induces an alternating sinusoidal current in the receiver coil. By gradient coils, a linearly changing magnetic field is used to spatially localise protons in one predetermined plane, since the frequency will correlate to the location. The registered signal constitutes of all co-registered frequencies and is stored in ‘k-space’ in rows ( $k_x$ ), i.e. frequency encoding (Figure 9).

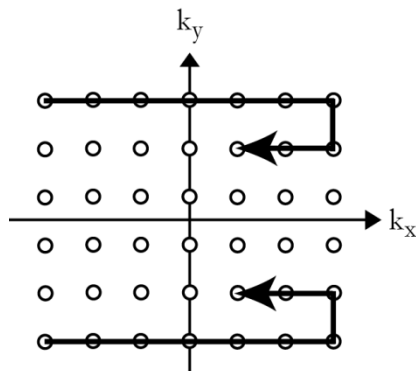


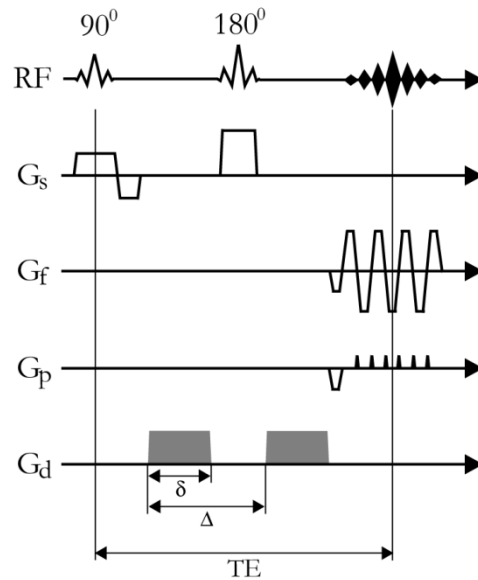
Figure 9. The registered MR signal is stored in k-space. Examples of k-space traversed from top to bottom and the reverse.

To localise protons in a second dimension the signal is sampled multiple times, each time changing the strength of the gradient magnetic field in this dimension. The registered signal is stored in further rows in k-space and consequently there is a pseudo frequency in the other axis ( $k_y$ ), i.e. phase-encoding. Via Fourier transformation, k-space is reconstructed to an image. There are several ways of collecting k-space, e.g. the above described rectilinear non-EPI (echo planar imaging) and others as EPI, radial and spiral.

## 2.3 DIFFUSION-WEIGHTED IMAGING

In 1986 Le Bihan *et al* showed that diffusion-weighted imaging (DWI) *in vivo* can be used to visualise random translational movement of water molecules, i.e. diffusion<sup>11</sup>. In DWI a T2-weighted spin echo sequence is used together with gradient pulses. Without diffusion-weighting each voxel has the signal intensity  $S_0$ . Short strong gradient pulses, i.e. linear magnetic field variation, are used to accomplish diffusion-weighting. The gradient pulse induces a position dependent phase change of protons. A short pause follows to allow the water molecules to move (diffuse). After the pause an equivalent, but inverted gradient pulse is applied. Between the gradient pulses the refocusing  $180^\circ$  RF pulse is applied, consequently both gradient pulses are in the same direction (Figure 10).

Figure 10. A pulse diagram of a diffusion-weighted sequence. RF: radiofrequency pulse;  $G_s$ : slice-selective gradient;  $G_f$ : frequency-encoding gradient;  $G_p$ : phase-encoding gradient;  $G_d$ : diffusion gradient;  $\delta$ : diffusion gradient duration;  $\Delta$ : diffusion gradient interval; TE: echo time.



Depending on the distance the water molecules have moved from their initial position, they will be exposed to a different magnetic field gradient. The initial phase will thereby not be restored, which results in a lower signal intensity,  $S_1$ .

$$S_1 = S_0 e^{-(TE/T2)} e^{-bD} \quad [4]$$

TE=echo time, T2=T2 relaxation time, b='diffusion-sensitising factor', D=diffusion coefficient.

Diffusion of water molecules is described statistically by a displacement probability distribution<sup>6</sup>. In biological tissue this Gaussian distribution is not correct, due to barriers (e.g. membranes, organelles), membrane permeability, intra- and extracellular space, cellularity and viscosity<sup>12,13</sup>. D is therefore called ADC (apparent diffusion coefficient), although the exact mechanisms correlating diffusion and physiological parameters are not fully known<sup>12</sup>. The 'diffusion-sensitising factor', i.e. the b-value, is shown in Eq. [5].

$$b = \gamma^2 G^2 \delta^2 (\Delta - \delta/3) \quad [5]$$

The b-value depends on  $\gamma$ =gyromagnetic ratio, G=diffusion-encoding gradient strength,  $\delta$ =diffusion-encoding gradient duration and  $\Delta$ =diffusion-encoding gradient interval (Figure 10). The b-value accounts for the degree of diffusion-weighting and is user-dependent. As a consequence of a higher b-value there is loss of signal, thus a lower signal-to-noise ratio (SNR). Diffusion, ADC (D), can be calculated using the signal intensities  $S_1$  and  $S_0$ , and the b-values.

$$D = \text{ADC} = \frac{\ln(S_1/S_0)}{b_1 - b_0} \quad [6]$$

To illustrate how the measured signal intensity depend on ADC, assume  $b_0=0$ , which is common in DWI, and rearrange Eq. [6] into Eq. [7].

$$S_1 = e^{-b_1 \cdot \text{ADC}} \cdot S_0 \quad [7]$$

From Eq. [7] it is noted, that if there are two types of tissues with the same  $S_0$  and the same b-value is used, tissues with a high ADC will have a lower  $S_1$  compared to tissues with a low ADC. However, tissues can have different  $S_0$  (a T2-weighted sequence is used). In a graph with the logarithmic signal intensity plotted on the vertical axis and the b-value on the horizontal axis, a higher ADC will be illustrated as a steeper curve (Figure 11).

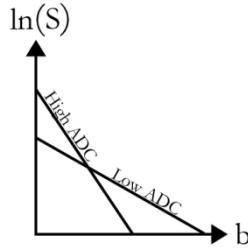


Figure 11. A logarithmic diagram illustrating that tissue with high ADC loses signal faster than tissue with low ADC, independently of b-value. However, this is not true for very high b-values.

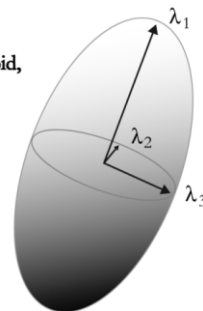
In brain imaging, a b-value of  $1000 \text{ s/mm}^2$  is considered optimal<sup>14,15</sup>. T2 relaxation time in muscles is much shorter compared to brain tissue. Since the diffusion-weighted sequence is based on a T2-weighted sequence, a consequence of the shorter T2 relaxation time is a lower SNR in the extremities<sup>14</sup>. Thus, DWI performed in the extremities compared to the brain, can be more difficult, since DWI is a technique suffering from low SNR<sup>16,17</sup>. Since DWI measures microscopic water molecule movement, it is also very sensitive to patient motion. The fastest sequence filling k-space, thus minimising patient motion during k-space collection, is EPI. This sequence traverses the entire k-space in one single collection. It was actually proposed by Sir Peter Mansfield in 1977 and was later proved to be useful in practice<sup>18</sup>.

The diffusion-encoding gradient is applied in a direction, e.g. anterior-posterior. To assess diffusion independent of the direction, it is measured in 3 orthogonal directions and summed, which is called the trace. By dividing the trace by three, the average ADC is calculated, which is called the mean diffusivity (MD).

## 2.4 DIFFUSION TENSOR IMAGING

If diffusion is equivalent in all directions (e.g. in pure water) it is isotropic. Most of the body tissue is inhomogeneous and diffusion is therefore not uniform in all directions, consequently it is anisotropic. In 1994 Basser *et al* described DTI to image anisotropic diffusion<sup>19</sup>. In each voxel diffusion is measured in at least 6 unique (non-collinear) directions plus a reference without diffusion-weighting. Subsequently a tensor is calculated, which represents diffusion in 3 dimensions. The tensor is often visualised as an ellipsoid (Figure 12).

Figure 12. A diffusion tensor represented by an ellipsoid, with its three eigenvectors  $\lambda$ .





The diffusion tensor ellipsoid is represented by 3 orthogonal eigenvectors (ordered as  $\lambda_1 \geq \lambda_2 \geq \lambda_3$ ), each having an eigenvalue.  $\lambda_1$  is the eigenvector correlating to the largest eigenvalue. Different properties of the tensor can be calculated, e.g. fractional anisotropy (FA), which displays the degree of anisotropy (total anisotropy FA=1 and isotropy FA=0).

$$FA = \sqrt{\frac{3}{2} \frac{(\lambda_1 - \bar{\lambda})^2 + (\lambda_2 - \bar{\lambda})^2 + (\lambda_3 - \bar{\lambda})^2}{\lambda_1^2 + \lambda_2^2 + \lambda_3^2}} \quad [8]$$

The diffusion measured in one direction, e.g. x-axis, is also dependent on the other directions, which is taken into account in the tensor calculation<sup>12</sup>.

### 2.4.1 Nerves and DTI

In 1990 Moseley *et al* showed that diffusion is anisotropic in white matter in the central nervous system of cat<sup>20</sup>. In two different studies in 1991, Moseley<sup>21</sup> *et al* and Hajnal<sup>22</sup> *et al*, showed that diffusion in (human) peripheral nerves also is anisotropic. Nerve diffusion is anisotropic due to their tubular structure, with the highest diffusion ( $\lambda_1$ ) parallel with the nerve, while it is restricted perpendicular to the nerve<sup>6,21</sup>. Although there is no exact explanation for diffusion anisotropy seen in nerves, it is considered to be due to hindrance of water molecules perpendicular to the membranes in the densely packed axons. Myelin sheaths could modulate anisotropy, although it has been hard to assess to what degree, while axonal transport and microtubules does not contribute to anisotropy<sup>23-25</sup>. Diffusion within the axon is similar in a parallel and perpendicular direction, i.e. isotropic, whereas when several axons are included it is anisotropic<sup>25</sup>. Diffusion anisotropy measures, e.g. FA, depend on several factors, e.g. axon diameters, axon number, axon orientation and degree of myelination<sup>26,27</sup>. There is a weak correlation ( $R^2=0.24$ ) between FA and mean axon diameters<sup>26</sup>.  $R^2>0.2-0.4$  is considered a fair correlation<sup>28</sup>. According to Eq. [8] a decrease in nerve FA is due to increased perpendicular diffusion, decreased parallel diffusion or both.

The voxel size used in clinical MRI studies is in a millimeter scale. The myelinated axon diameter is approximately 4-10  $\mu\text{m}$ , the myelin 0.5-2  $\mu\text{m}$  thick with 0.5-2  $\mu\text{m}$  extraaxonal separation<sup>4</sup>. If a maximum axon diameter, myelin thickness and extraaxonal separation is assumed, the ‘total diameter’ for each axon is approximately 14  $\mu\text{m}$  and if the minimum is assumed, it is approximately 5  $\mu\text{m}$ . Using a simple approximation, a 1.0  $\text{mm}^3$  voxel (since the nerves are running parallel, the area for nerve fibers is 1  $\text{mm}^2$ ) will contain approximately 5100-40000 parallel axons, including other tissues, e.g. collagen and fat.

### 2.4.2 Fractional anisotropy colour encoded images and fiber tracking

Tensor information can be visualised in different ways, e.g. fractional anisotropy colour encoded image maps (FA-CEI) with colours corresponding to the direction of the first eigenvector ( $\lambda_1$ ). Green corresponds to anterior-posterior diffusion (y-axis); red to left-right (x-axis) and blue to superior-inferior (z-axis). Another approach is fiber tracking/tractography, first shown in 1999 by Mori<sup>29</sup> *et al.* It generates 3-dimensional fibers by joining tensor information in adjacent voxels, according to user-defined parameters. It is based on the  $\lambda_1$ -direction which correlates to the nerve direction. An array of different software programs for fiber tracking exists, both vendor-supplied and freely available on the internet<sup>30</sup>.

### 2.4.3 Compartments

Body tissue can be divided into intra- and extracellular volumes, i.e. two different compartments. In the body approximately 80% is intracellular volume and 20% is extracellular volume. Intracellular volume is more viscous, since it contains more proteins. However, the diffusion signal cannot be explained by these two compartments<sup>12</sup>.

The diffusion signal *in vivo* does not have a mono-exponential decay. However, it is unclear if it fits best with a bi-exponential decay, a tri-exponential decay or with other models<sup>12,31,32</sup>. The two compartments, intra- and extracellular volume, cannot explain the bi-exponential decay<sup>12</sup>. A two water pools model has been proposed as an explanation for bi-exponential decay, with a slow (ADC  $0.3 \times 10^{-3}$  mm<sup>2</sup>/s) and fast (ADC  $1.3 \times 10^{-3}$  mm<sup>2</sup>/s) component, in slow or intermediate exchange<sup>31</sup>.

## 2.5 MAGNETIC FIELD

Improving SNR is of great importance, since DWI and DTI inherently are suffering from low SNR, which will affect both precision and accuracy<sup>16,33</sup>. Diffusion itself is independent of the external magnetic field strength, albeit an indirect effect can be seen, due to the altered T1 and T2 relaxation times<sup>14</sup>. SNR theoretically doubles from 1.5 T to 3.0 T, since it varies linearly with the external magnetic field. However, tissue T1 relaxation time increases with a higher magnetic field and TR consequently has to be prolonged, otherwise SNR gain is impaired. At 3.0 T compared to 1.5 T, the T2 relaxation decreases, although to a lesser extent, necessitating only a slightly shorter TE. At 3.0 T compared to 1.5 T, the T1 relaxation time in muscles increases approximately 20% and the T2 relaxation time decreases approximately 10%<sup>34</sup>. In diffusion measurements in calf muscles, doubling from 1.5 T to 3.0 T, whilst using nearly identical MRI protocols, results in

a SNR increase by a factor of  $1.64^{14}$ . The specific absorption rate, i.e. energy deposition, increases with the square related to the magnetic field, thus will it quadruple from 1.5 T to 3.0 T<sup>35</sup>.

## 2.6 MAGNETISATION TRANSFER IMAGING

Magnetisation transfer imaging utilises that body water is within two magnetisation pools, a mobile and a non-mobile water pool, which are in magnetisation equilibrium. Non-mobile water, which is not imaged in conventional MRI sequences, is bound to macromolecules, e.g. myelin. By applying an off-resonance RF pulse, saturating the non-mobile pool, the mobile water will exchange magnetisation and the measured signal will decrease. When comparing the signal measured in an identical sequence, with and without an off-resonance pulse, magnetisation transfer ratio (MTR) can be calculated<sup>36,37</sup>. Reduced MTR compared to normative values, indicates a reduction in free water magnetisation exchange. This is non-specific, but in white matter in multiple sclerosis it is related to axon damage and myelin content, i.e. demyelination<sup>36,38</sup>. However, MTR is also correlated to inflammation and oedema<sup>39</sup>. MTR has been evaluated *in vivo* in human normal nerves<sup>40,41</sup>, although so far no studies are published on peripheral nerve pathology.

## 2.7 PARKINSON'S DISEASE

Parkinson's disease (PD) is a progressive neurodegenerative movement disorder<sup>42,43</sup>. It primarily affects the elderly and the incidence thereafter quickly rises with age. Approximately 10% of patients are below 45 years of age<sup>43</sup>. It is a clinical diagnosis characterised by motor symptoms, i.e. tremor (4-6 cycles/second), rigidity and bradykinesia, often being asymmetric<sup>42-44</sup>. Patients with newly diagnosed PD should response to levodopa treatment<sup>44</sup>. There is accumulating evidence that certain non-motor symptoms, such as hyposmia, rapid eye movement (REM) sleep behaviour disorder, constipation and depression precede the motor symptoms by several years<sup>45</sup>. The patient and family members have often retrospectively noticed, after the PD diagnosis, symptoms and signs going back for more than a decade<sup>43</sup>. Even dementia and dysautonomia are frequent in the disease, especially in late stages<sup>42</sup>.

PD is a synucleinopathy, which characteristically involves pars compacta of substantia nigra (SN), although histopathological data suggests that PD initially affects the olfactory bulb (OB) and the dorsal motor nucleus of the vagal nerve<sup>9</sup>. The cause of the disease is still unclear and few environmental factors have been found. It is likely that PD already existed in the preindustrial era. Susceptibility

genes have been found and caffeine, an adenosine A2 receptor antagonist, seems to have a protective effect<sup>43</sup>.

In parkinsonism, i.e. symptoms seen in PD, structural MRI can reveal other diagnoses, e.g. tumours in the basal ganglia or thalamus, normal pressure hydrocephalus, Creutzfeldt–Jakobs disease or manganism<sup>46</sup>. Vascular parkinsonism show on MRI extensive subcortical white-matter ischaemic changes<sup>43</sup>. Other differential diagnoses in parkinsonism are the much more unusual movement disorders progressive supranuclear palsy, multiple system atrophy and corticobasal degeneration. Single-photon emission computed tomography (SPECT) using <sup>123</sup>I-Ioflupane (DaTSCAN) can be used in PD diagnostics. <sup>123</sup>I-Ioflupane has affinity to the dopamine transporter, a presynaptic protein regulating dopamine concentration in the synaptic cleft<sup>47</sup>. In PD there is a reduction of uptake in the putamen, a specific brain region<sup>48</sup>. However, DaTSCAN cannot effectively differentiate between PD, progressive supranuclear palsy, multiple system atrophy and corticobasal degeneration<sup>47</sup>. DaTSCAN can strengthen the PD diagnosis, since only 4-14% of patients with early onset of disease have normal scans<sup>43</sup>. On conventional MRI, multiple system atrophy can show non-specific hypo/hyperintensities in the putamen and have atrophy of the pons and cerebellum. Indicative for multiple system atrophy is the ‘hot cross bun’ sign, which is a cruciform hyperintensity seen in the pons in T2-weighted images<sup>43,46</sup>. This is caused by atrophy and gliosis of transverse travelling pontocerebellar fibers<sup>46</sup>. Progressive supranuclear palsy can on conventional MRI show mesencephalon atrophy, recognised by the ‘hummingbird’ sign, and atrophy of the superior cerebellar peduncles. Olfaction impairment is generally not present in multiple system atrophy, progressive supranuclear palsy or vascular parkinsonism<sup>43</sup>.

On histopathological examination  $\alpha$ -synuclein-immunoreactive inclusions are seen in involved neurons in PD. In the brain, PD affects specific regions and specific neurons, but also the PNS, including the enteric nervous system. Within cell bodies  $\alpha$ -synuclein inclusions present as Lewy bodies and within cellular processes (axons and dendrites) as spindle-like Lewy neuritis. Neurons with long, thin unmyelinated axons or poorly myelinated axons are especially affected, e.g. the olfactory and nigrostriatal projecting neurons. To transmit impulses, unmyelinated and poorly myelinated axons require more energy than myelinated axons, which could make them more vulnerable to oxidative stress. Another factor making these neurons more vulnerable is the lesser interaction with oligodendrocytes, which produce and maintain myelin, making them more sensitive to pathological sprouting. Lewy inclusions are regarded as a continuous pathological process and six neuropathological stages have been defined, with stage 1-2 being preclinical. Lewy inclusions are not regarded as part of natural ageing and are not seen in all elderly. Dopaminergic nigrostriatal degeneration is a hallmark of PD, but other transmitter systems are affected as well. The various stages of PD affect different brain regions, starting in the lower brainstem and ending in the cerebral cortex,

although affected areas also continuously deteriorate. In stage 1 disease, the anterior olfactory nucleus in the OB and olfactory tract, and the dorsal motor nucleus of the vagus nerve are affected. In stage 3, pars compacta of the SN is involved, which will ultimately lead to the loss of neuromelanin containing neurons and consequently the loss of pigmentation upon histopathological examination. When the PD patient starts to develop discrete clinical symptoms, early synucleinopathy changes exist in the SN, and extensive changes in the dorsal motor nucleus of the vagus nerve, lower raphe nuclei and locus coeruleus<sup>9</sup>.

### 2.7.1 Hyposmia

There are many entities causing hyposmia and anosmia, e.g. congenital, post-infectious, post-traumatic, chronic rhinosinusitis, idiopathic, tumours or neurodegenerative disorders<sup>7,49</sup>. Despite the prior assumption of post-natal neurogenesis in human OBs<sup>7</sup>, which is seen in rodents and adult monkeys, a recent study showed none or very limited<sup>50</sup>.

An easy method to test smell, without using complex equipment for threshold testing, is odor detection with the University of Pennsylvania Smell Identification Test (UPSIT). The correlation of UPSIT and threshold detection is high<sup>51</sup>. UPSIT has high test-retest reliability. The 40-item UPSIT consists of four booklets, each containing 10 stimuli of ‘scratch and sniff’ odorants. For each stimulus the participant is prompted to choose one of four options. The result is compared with normative data (age and gender), and the participants are scored as normosmic, mild microsmic, moderate microsmic, severe microsmic, anosmic or probable malingering (<http://sonsonics.com/sit-administration-manual.html>). Healthy women as a group, perform better than men on UPSIT, which also is evident in other studies<sup>51</sup>.

In some clinical entities, e.g. post-traumatic and congenital disorders, decreased OB volume correlates with olfactory sensitivity. However, accurate measurements of the thin OBs are difficult and the variation among healthy individuals is large<sup>52</sup>. No OB volume difference has been observed in PD patients compared to healthy controls<sup>53</sup>.

## 2.8 SPINOCEREBELLAR ATAXIA

Spinocerebellar ataxia (SCA) is a heterogeneous group of autosomal dominant neurodegenerative disorders<sup>54,55</sup>. So far, 36 SCA types have been described, each type caused by mutations in a specific gene or associated with a specific chromosome region (<http://neuromuscular.wustl.edu/ataxia/domatax.html>). Progressive ataxia, i.e. loss of coordination, is the most common first symptom,

with onset usually at 30-50 years of age. Additional non-ataxia symptoms are common and depend on the type<sup>55</sup>. The SCA prevalence in Europe is approximately 1-3/100 000. SCA1, 2, 3, 6 and 7 are the most common, while the other types are considered rare. Globally SCA3, also known as Machado-Joseph disease (MJD), is the most common type<sup>54,56</sup>. Varying degrees of cerebellar degeneration are seen in all types<sup>54</sup>. Involvement of other structures such as basal ganglia, brainstem, spinal cord, retinae and peripheral nerves differ between the types<sup>54,56</sup>. Brainstem degeneration appears to be most important in SCA1, both brainstem and cerebellum become atrophic in SCA3/MJD, while only the cerebellum is involved in SCA6<sup>54,57,58</sup>. The PNS is involved in approximately 50% of SCA1, 80% of SCA2 and commonly seen in SCA3/MJD<sup>54,58</sup>. Atrophy of the spinal cord has only been described in SCA3/MJD<sup>59</sup>.

### 3. MATERIAL AND METHODS

#### 3.1 HEALTHY INDIVIDUALS AND PATIENTS

In **Study I** the proximal part of the left sciatic nerve was examined in three healthy individuals. In **Study II** the distal part of the left sciatic nerve was examined in three healthy individuals. In **Study III** the ‘olfactory nerves’ were examined in five healthy individuals and one patient with congenital anosmia. In **Study IV** the OB, SN and corpus callosum (CC) were examined in 16 healthy individuals and 18 PD patients. To strengthen the validity of the PD diagnosis all PD patients underwent DaTSCAN quantified with BRASS software<sup>48</sup>. Asymmetry index was calculated for putaminal uptake, i.e. comparison of the left and right side.  $\text{Asymmetry index} = (\text{higher SPECT signal} - \text{lower SPECT signal}) / (\text{higher SPECT signal}) \times 100$ . Symptoms of the PD patients were scored according to Hoehn & Yahr and Unified Parkinson Disease Rating Scale. Unpaired two-tailed Student’s *t* test was used for statistical analyses (GraphPAD Prism 4.0; USA). A  $p < 0.05$  was considered significant. In **Study V** the brain, spinal cord and left distal sciatic nerve were examined in four patients of the Swedish ‘Huddinge SCA Family’ and in four age- and gender-matched healthy controls. All patients underwent electroneurography (ENeG) and patient#1 underwent a sural nerve biopsy. All patients were scored according to the Scale for the assessment and rating of ataxia (SARA)<sup>60</sup>. Pearson coefficient was calculated for correlation of SARA scores with MRI measurements. A  $p < 0.05$  was considered significant. Age and gender data is presented in Table 1.

Patient/Control	Age (years)	Gender	SARA
#1	70/71	male/male	11.5
#2	60/63	female/female	17.5
#3	75/77	male/male	20
#4	32/33	male/male	1.5

Table 1. Age and gender for patients and healthy controls in Study V.  
SARA scores for patients.

#### 3.2 MR-SCANNERS

In **Study I, II, III** and **IV** a 1.5 Tesla MR-scanner (Gyrosan Intera; Philips Medical Systems, Best, The Netherlands) was used. In **Study V** a 3.0 Tesla MR-scanner (Magnetom VERIO, Siemens Healthcare) was used for the spinal cord and left distal sciatic nerve and a different 3.0 Tesla MR-scanner (Discovery MR750, General Electric) was used for the brain.

### 3.3 COILS

In **Study I** and **II** a 2-channel phased-array coil was used. In **Study III** and **IV** a multi-channel phased-array head coil was used. In **Study V** a transmit/receive 15-channel knee coil, a 32-channel spine coil and a 32-channel head coil were used.

### 3.4 DIFFUSION-WEIGHTED SEQUENCES

#### Study I

A diffusion-weighted sequence was performed in an axial plane with a single-shot diffusion-weighted EPI sequence, b-value  $400 \text{ s/mm}^2$  in 32 vendor-supplied diffusion encoded directions plus a reference image without diffusion-weighting [TE=70 ms, TR=4 s, slice thickness/gap=6/0 mm, 25 slices, field of view (FOV)= $24 \times 24 \text{ cm}$ , matrix= $96 \times 96$ , voxel size= $2.5 \times 2.5 \times 6.0 \text{ mm}$ ].

#### Study II

A diffusion-weighted sequence was performed in an axial plane with a single-shot diffusion-weighted EPI sequence, b-value  $1000 \text{ s/mm}^2$  in 36 in-house diffusion encoded directions plus a reference image without diffusion-weighting [TE=87 ms, TR=6698 ms, slice thickness/gap=4/0 mm, 30 slices, FOV= $22 \times 22 \text{ cm}$ , matrix= $96 \times 128$ , voxel size= $2.3 \times 1.7 \times 4.0 \text{ mm}$ , number of signal averages (NSA)=6]. Sensitivity encoding (SENSE) with an acceleration factor of 2 was used. Spectral presaturation with inversion recovery (SPIR) was used for fat suppression. The first of the 36 diffusion-encoded gradient directions was solely in the z-direction, i.e. proximal-distal direction. The following gradient directions were repeated with a  $5^\circ$  inclination, resembling a fan, in the phase-encoding direction, i.e. in an anterior-posterior plane, until the complete plane was covered (Figure 13).

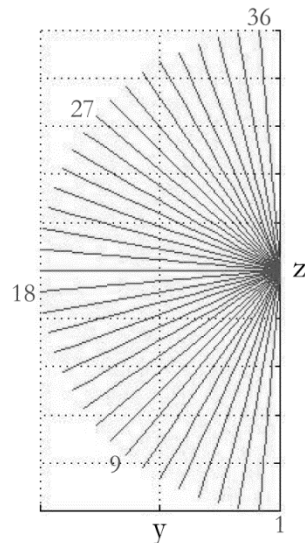


Figure 13. The 36-gradient diffusion direction scheme; y-axis, anterior-posterior direction; z-axis proximal-distal direction.



## Study III

A diffusion-weighted sequence was performed in an axial plane with a single-shot diffusion-weighted EPI sequence, b-value  $900 \text{ s/mm}^2$  in 32 vendor-supplied diffusion encoded directions plus a reference image without diffusion-weighting [TE=83 ms, TR=6698 ms, slice thickness/gap=3/0 mm, 26 slices, FOV=23×23 cm, acquisition matrix=128×128, reconstruction matrix=256×256, voxel size=0.9×0.9×3.0 mm, NSA=4, partial Fourier encoding=0.6]. A SENSE-factor of 2.1 and SPIR was used for fat suppression. The diffusion sequence time was 13.31 minutes. Post-processing with eddy current/motion correction and b-matrix reorientation was performed using software tools from the FMRIB software library (<http://www.fmrib.ox.ac.uk/fsl>) provided by FSL.

## Study IV

A diffusion-weighted sequence was performed in an axial plane with a single-shot diffusion-weighted EPI sequence, b-value of  $900 \text{ s/mm}^2$  in 32 vendor-supplied diffusion encoded directions plus a reference image without diffusion-weighting [TE=83 ms, TR=6698 ms, slice thickness/gap=3/0 mm, 26 slices, FOV=23×23 cm, acquisition matrix=128×128, reconstruction matrix=256×256, voxel size=0.9×0.9×3.0 mm, NSA=4, partial Fourier encoding=0.6]. A SENSE-factor of 2.1 and SPIR was used for fat suppression. The diffusion sequence time was 13.31 minutes. By using software tools from the FMRIB software library (<http://www.fmrib.ox.ac.uk/fsl>), diffusion-weighted images were visually analysed for head movements in three reconstructed planes. Diffusion-weighted images were then post-processed with eddy current/motion correction and b-matrix reorientation. For each voxel, tensor components were calculated, i.e. eigenvectors, eigenvalues, FA and MD, and FA-CEI were reconstructed. The intra-individual variability was tested by performing two identical diffusion-weighted sequences and calculating the coefficient of variation  $CV = \text{std}(x_i) / \text{mean}(x_i)$ .

## Study V

A diffusion-weighted sequence was performed in an axial plane with a single-shot diffusion-weighted EPI sequence, b-value of  $1000 \text{ s/mm}^2$  in 30 vendor-supplied diffusion encoding directions plus a reference image without diffusion-weighting [TE=85 ms, TR=3000 ms, slice thickness/gap=5/5 mm, slices=10, FOV=15.5×15.5 cm, acquisition matrix=124×124, voxel size=1.2×1.2×5.0 mm, NEX=6, partial Fourier encoding=5/8.] Generalised autocalibrating partially parallel acquisition with an acceleration factor of 3 was used. Spectral adiabatic inversion recovery (SPAIR) for fat suppression was used. FA-CEI were calculated on a voxel-by-voxel basis. Using T2-weighted images for anatomical reference, a circular regions of interest (ROI) approximately 6 mm in diameter, was placed in

the sciatic nerve on FA-CEI. The highest FA value was recorded in each slice and a mean value was calculated for each patient.

### 3.4.1 Fiber tracking

#### **S**study I

Fiber tracking was performed with an IDL-based (Research Systems INC., Boulder, CO, USA) fiber tracking program (PRIDE) provided by Philips. Fiber tracking constraints were made with ROIs placed surrounding the expected anatomical place for the sciatic nerve in two axial slices. The largest fiber deviation in one step was  $9.4^\circ$ , minimum fiber length was 80 mm, with a step size of 0.5 voxel. FA threshold was set to 0.3.

#### **S**study III

Software tools provided by Bioimage Suite were used for fiber tracking<sup>61</sup>. Fiber tracks were calculated using a fourth order method Runge-Kutta algorithm. Fiber tracking was initiated with a ROI placed in the expected anatomical place for each of the olfactory tracts. Largest fiber deviation in one step was  $10^\circ$ , minimum fiber length was 5 mm, with a step size of 0.25 voxel. FA threshold was set to 0.18.

### 3.4.2 Diffusion-direction-dependent imaging

#### **S**study II

Two methods for nerve visualisation were tested:

1. A method using diffusion-weighted raw image data from a single diffusion direction was used. With diffusion direction perpendicular to the nerve direction the signal is preserved, while a diffusion direction along the nerve attenuates the signal. Due to the course of the nerve, direction 18 (Figure 13) was perpendicular and therefore used. Maximum-intensity projection (MIP) images were used to present data, without and with a ROI surrounding the nerves to exclude other tissues.

2. A method called diffusion-direction-dependent imaging (DDI), combining diffusion-weighted raw image data from all 36 diffusion directions via a simple post-processing model. For each acquired voxel, signal intensity was plotted on the y-axis and the diffusion directions on the x-axis. The signal intensities in a voxel varied with the diffusion direction and were tissue-dependent (Figure 14).

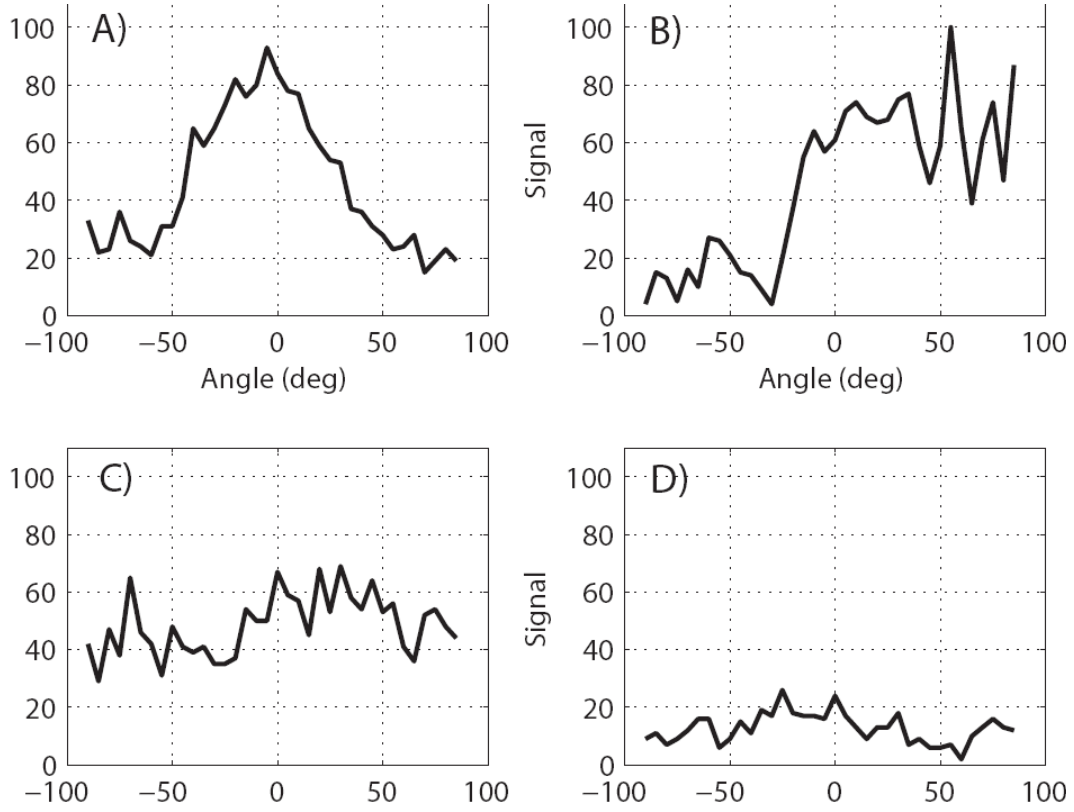


Figure 14. Graphs illustrating signal intensities varying over the spatial angle in voxels of different tissues. (A) Sciatic nerve. (B) Vessel. (C) Chemical shift artifact. (D) Muscle.

An expected curve shape ( $\hat{x}$ ) of a nerve was calculated by selecting 10 voxels from each three subject's sciatic nerve, yielding a total of 30 curves. The 10 voxels from each subject were manually depicted by selecting one voxel in every third axial diffusion image. All voxels were selected from direction 18 (Figure 13). In distal slices, voxels of either the common peroneal nerve or the tibial nerve were used. All curves were normalised to one, and the mean expected curve was calculated and smoothed using a three-point Gaussian sliding window (Figure 15).

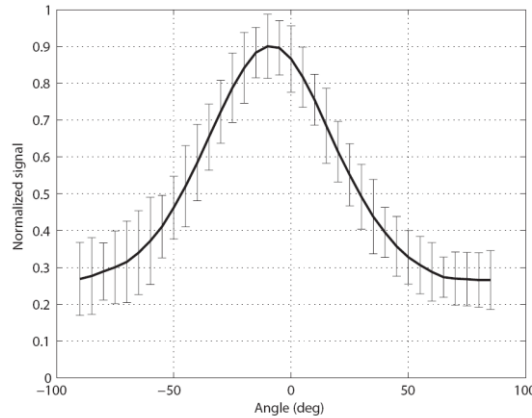


Figure 15. The mean expected curve shape for a nerve calculated in three healthy subjects. The normalised diffusion signal and the standard deviation for each angle are shown. The peak of the curve is slightly shifted to negative angles due to there being most perpendicular to the nerve fiber directions.

In order to visualise the nerve and to suppress all other tissues, a comparison between the expected curve shape ( $\hat{x}$ ) and the measured curve shape was made voxel per voxel, as shown in Eq. [9] and [10].

$$\varepsilon_{\rho}(\delta) = \sum_{n=1}^N \left| \frac{\hat{x}(n+\delta) - x_{\rho}(n)}{\hat{x}(n+\delta)} \right| \quad [9]$$

$$y_{\rho} = \min \{ \varepsilon_{\rho} \} \quad [10]$$

$n$  is the diffusion direction index and  $N$  is the number of diffusion directions.  $x_{\rho}(n)$  is the MR signal in voxel  $\rho$  along direction  $n$ .  $\hat{x}$  is the expected curve shape from a nerve fiber, scaled to  $x_{\rho}$  with least squares estimation.  $\delta$  is the offset in the diffusion direction index compensating for the direction of the nerve, and  $\varepsilon_{\rho}$  is the error sum between  $\hat{x}$  and  $x_{\rho}$ .  $y_{\rho}$  is the minimum error sum of  $\varepsilon_{\rho}$  in voxel  $\rho$ .  $y_{\rho}$  was calculated for every voxel in the imaged volume and was used as contrast in post-processed images, i.e. DDI images.

### 3.4.3 Inherent diffusion directional information

#### **S**study IV

Two methods were used for localisation and analysis:

1. A method for OB. OBs were localised in T2-weighted images (Figure 16A, B) and correlated to proton density-weighted images and FA-CEI (Figure 16C).

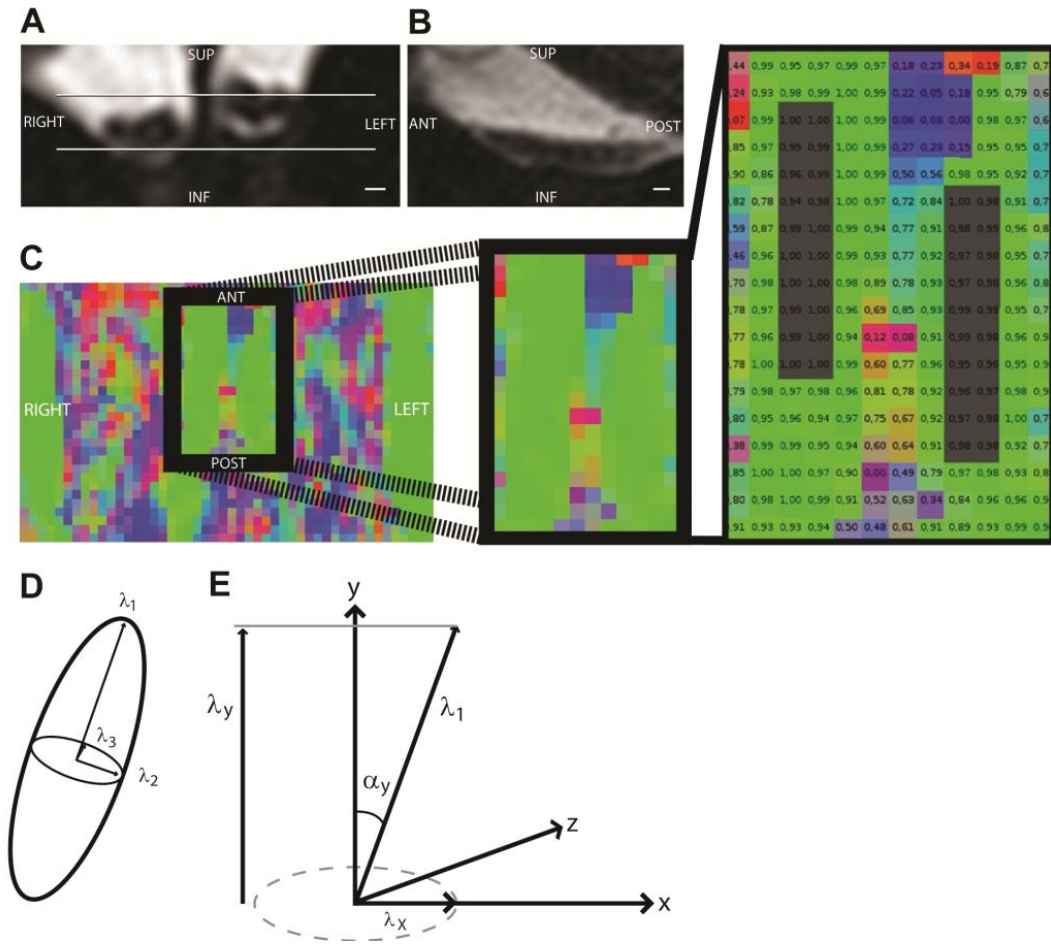


Figure 16. A) Coronal T2-weighted MRI image with lines corresponding to an axial DTI slice covering OBs. B) Sagittal T2-weighted MRI image of an OB. C) Axial FA colour encoded images with OBs (box) and both medial rectus muscles visualised in green colour. Magnification images of the OBs with  $\lambda_y$  for each voxel. In grey colour ROIs (left and right) with highest ROI mean  $\lambda_y$  value. D) Tensor with eigenvectors. E) Eigenvector  $\lambda_1$  with its  $\lambda_y$  and  $\lambda_x$  components and  $\alpha_y$  angle. SUP: Superior; INF: Inferior; ANT: Anterior; POST: Posterior. Scale bar=1 mm in A, B.

OB location correlated to green in FA-CEI (Figure 16C).  $\lambda_1$  is normalised to 1 and consists of three specific values in 3D space; y-axis ( $\lambda_y$ ), x-axis ( $\lambda_x$ ) and z-axis ( $\lambda_z$ ) (Figure 16D, E). If  $\lambda_1$  equals 1 in the y-axis ( $\lambda_y$ ) the tensor is directed solely in the y-axis. If  $\lambda_y < 1$  then  $\lambda_1$  is deviating with an angle  $\alpha_y$  from the y-axis (Figure 16E). Since  $\lambda_1$  is normalised to 1, the angle  $\alpha_y = \arccos \lambda_y / \lambda_1 = \arccos \lambda_y$ . Absolute values of  $\lambda_y$  of the  $\lambda_1$  were plotted in FA-CEI at the location of both OBs (Figure 16C; values retrieved by tensor calculations can be negative or positive, but the diffusion direction cannot be judged being anterior or posterior). A high value  $\lambda_y$ , which corresponds to a small deviating  $\alpha_y$  angle, indicates diffusion directed in the y-axis which correlates to the OB direction. A rectangular ROI (2×10 voxels; 1.8×9 mm) was placed in each OB at the location where the mean value of the ROI had the highest  $\lambda_y$  value (Figure 16C, E). The ROI for each OB was used to calculate mean FA, mean MD, mean  $\lambda_y$  and mean  $\alpha_y$  angle. In each individual, the OB (left or right) with the highest ROI  $\lambda_y$  mean value (corresponding to the smallest  $\alpha_y$  angle) was selected for analysis, since this has the highest association to the anterior-posterior direction of the OB and is least influenced by partial volume effects. The largest

transaxial diameters of OB were measured on coronal T2-weighted images and length on sagittal images (Figure 16A, B). Due to the shape of the OB an ellipsoid volume calculation ( $4/3 \cdot \pi \cdot ((x/2) \cdot (y/2) \cdot (z/2))$ ) was used.

2. A method for SN. SN is located close to the cerebral peduncle just below the level of the inferior part of the red nucleus<sup>62</sup>. A proton density-weighted sequence was used to find the correct level of SN in mesencephalon. By using the b-zero image and FA-CEI, bilateral ROIs were placed at the SN and its junction to the cerebral peduncle, corresponding to the blue-green interface on FA-CEI. Each ROI consisted of three 5×2 voxels subROIs (Figure 17).

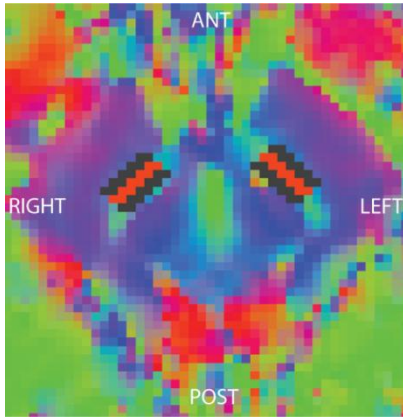


Figure 17. An axial FA colour encoded MRI image. Three subROIs (black, orange, black) on each side at the location of SN adjacent to the cerebral peduncle. ANT: Anterior; POST: Posterior.

The cerebral peduncles have their nerve fibers and diffusion directed in the z-axis. The mean  $\lambda_z$  was therefore calculated for each subROI. A high value for mean  $\lambda_z$  indicates nerve fibers travelling in a superior-inferior direction, i.e. the cerebral peduncle. A cut-off mean value  $\lambda_z$  over 0.6 was empirically used to assume that the subROI was located at the interface of the cerebral peduncle and SN, with even higher value  $\lambda_z$  in the cerebral peduncle. The next inner subROI, on each side, was used for SN analysis and to calculate mean FA, mean MD and mean  $\lambda_y$ .

For comparison, the trunk of the CC<sup>63</sup> with its nerve fibers and diffusion direction in the x-axis was used. It was localised in FA-CEI and a quadratic ROI (10×10 voxels; 9×9 mm) was placed in both series in the same place in region II-III, according to Hofer and Frahm<sup>64</sup>. For each ROI mean FA, mean MD and mean  $\lambda_x$  was calculated.

### 3.5 MAGNETISATION TRANSFER SEQUENCE

#### Study V

Magnetisation transfer imaging was performed, without and with an off-resonance RF pulse (1.5 kHz off-resonance, 10 ms long Gaussian pulse, 500° effective flip angle) [TE=7 ms, TR=33 ms, flip angle=10, slice thickness/gap=5.0/1.0 mm, slices=20, FOV=15.4×15.4 cm, acquisition

matrix=192×192, voxel size=0.8×0.8×5.0 mm, NSA=5]. Mean MTR was calculated for each patient.  $MTR=100 \times (\text{magnetisation transfer imaging without} - \text{magnetisation transfer imaging with}) / \text{magnetisation transfer imaging without}$ . On magnetisation transfer images, without and with the RF pulse, a ROI approximately 6 mm in diameter was placed in identical positions as in FA-CEI, in the sciatic nerve. Due to proximal and distal fold-over artifacts in the magnetisation transfer images, the central 13 slices were used for analysis. A circular ROI, approximately 10 mm in diameter was placed in the vastus medius muscle and mean MTR was calculated for each patient.

### **3.6 T<sub>1</sub>-, T<sub>2</sub>- AND PROTON DENSITY-WEIGHTED SEQUENCES**

#### **S<sub>study I</sub>**

T<sub>2</sub>-weighted imaging in the axial plane was performed for anatomical reference.

#### **S<sub>study II</sub>**

T<sub>1</sub>-weighted imaging in the axial plane was performed for anatomical reference.

#### **S<sub>study III and IV</sub>**

T<sub>2</sub>-weighted driven-equilibrium imaging in the coronal and sagittal plane of the OB and olfactory tracts were performed for anatomical reference. Proton density-weighted imaging in the axial plane of the brain (from below of mesencephalon to above CC), with equal slice thickness and spatial resolution as the diffusion-weighted sequence, was performed for anatomical reference.

#### **S<sub>study V</sub>**

The brain was examined with a T<sub>1</sub>-weighted 3D fast spoiled gradient echo (FSPGR) BRAVO [TR=8.1 ms, TE=3.2 ms, FOV=256 mm, acquisition matrix=256×256, slices=176, slice thickness=1.0 mm, voxel size=1.0×1.0×1.0 mm, flip angle=12, prep time=450 ms, NEX=1], T<sub>2</sub>-weighted axial PROPELLER sequence [TR=3000 ms, TE=110 ms, FOV=240 mm, matrix=384×384, slice thickness=4.0 mm, voxel size=0.6×0.6×4.0 mm, NEX=1.5] and sagittal 3D CUBE FLAIR sequence [TR=6000 ms, TE=128 ms, FOV=240 mm, acquisition matrix=256×224, slices=292, slice thickness=1.2 mm, voxel size=0.9×1.1×1.2 mm, inversion time=1860 ms, NEX=1].

The spinal cord was examined with a sagittal T2-weighted sequence [TR=3000 ms, TE=102 ms, FOV=350 mm, acquisition matrix=512×384, slices=15, slice thickness/gap=3.0/0.3 mm, voxel size=1.0×0.8×3.0 mm, NEX=2].

The left distal thigh was examined with a 3D T2-weighted sequence [TR=1500 ms, TE=134 ms, FOV=178 mm, acquisition matrix=192×188, slices=96, slice thickness=1.0mm, voxel size=0.9×0.9×1.0 mm, NEX=2].

### **3.7 OLFACTION TESTING**

Olfaction was tested with the 40-item UPSIT.

### **3.8 MRI VOLUMETRY AND SPINAL CORD MEASUREMENTS**

#### **Study V**

The T1-weighted 3D FSPGR BRAVO sequence was used for MRI volumetry. Using software tools from the FMRIB software library (<http://www.fmrib.ox.ac.uk/fsl>), the brain was extracted from surrounding bone and segmented into brain tissue and cerebrospinal fluid. The brain was manually segmented into cerebrum, mesencephalon, pons, medulla oblongata and cerebellum<sup>65</sup>. The percentage of each structure, as part of the total brain volume was calculated. The midsagittal distance of the spinal cord was measured, at the midlevel of each vertebra from C1 to Th12, and mean value was calculated for each patient.

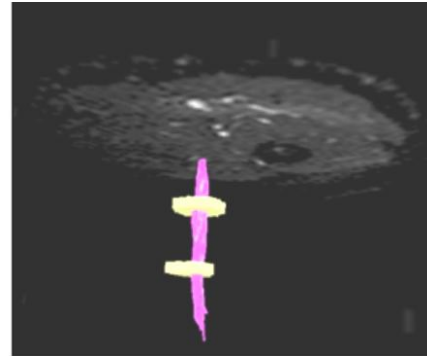


## 4. RESULTS

### 4.1 PERIPHERAL NERVE DIFFUSION TENSOR IMAGING

In **Study I** fiber tracking (Figure 18) of the diffusion tensor images detected a bundle of fibers in all 3 individuals. The location of the fibers correlated to the sciatic nerve.

Figure 18. Frontal view with the most proximal axial slice and the 2 ROIs used for fiber tracking of the sciatic nerve.



### 4.2 DIFFUSION-DIRECTION-DEPENDENT PERIPHERAL NERVE IMAGING

In all three subjects in **Study II**, the sciatic nerve and its division were visualised on unidirectional diffusion MIP images in a direction perpendicular (direction 18) to the sciatic nerve (Figure 19A). Chemical shift artifacts and artifacts from vessels partly obscured the nerves. By manually drawing a ROI over the course of the nerves, these artifacts could be excluded (Figure 19B). DDI images clearly visualised the sciatic nerve and its division (Figure 19C).

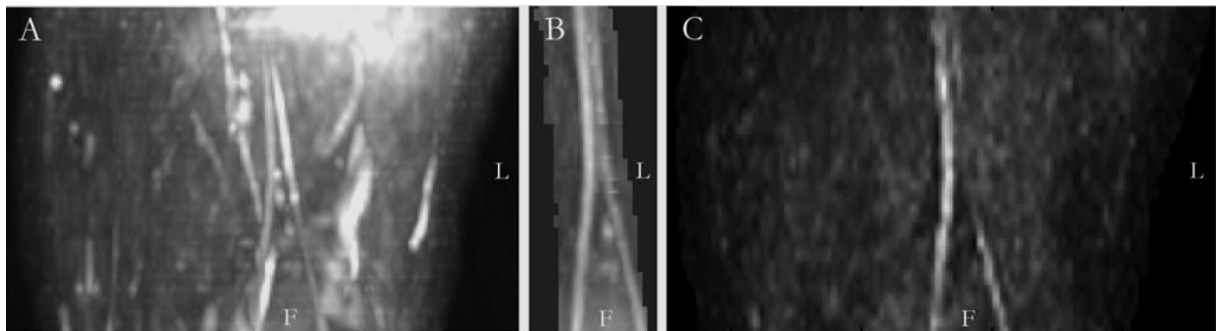


Figure 19. Coronal views in one of the participants. Unidirectional diffusion MIP image (direction 18) without (A), and with ROI (B) surrounding the course of the nerves. C) DDI image. L: Left; F: Feet.

### 4.3 DIFFUSION TENSOR FIBER TRACTOGRAPHY OF THE OLFACTORY TRACT

In **Study III**, OB and olfactory tracts were visualised in all five healthy individuals on T2-weighted images with corresponding fiber tracking (Figure 20). Mean of the maximum tracking length for the right side was 9 mm (5–11 mm) and for the left side 11 mm (7–14 mm). For the right side the mean FA range, derived from fiber tracking results, was 0.19–0.23 and for the left side it was 0.21–0.28. By contrast, in the anosmic patient neither OB nor olfactory tracts were visualised, neither on T2-weighted images nor on fiber tracking images.

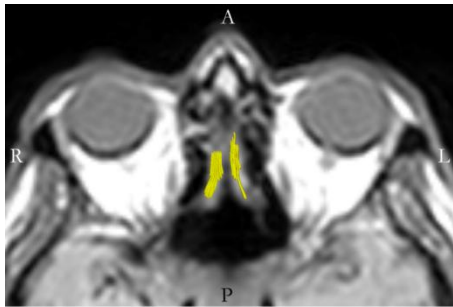


Figure 20. An axial proton density-weighted image with fiber tracked OBs and olfactory tracts (yellow colour). A: Anterior; R: Right; L: Left; P: Posterior.

### 4.4 MRI DIFFUSION IN PARKINSON'S DISEASE: USING THE TECHNIQUE'S INHERENT DIRECTIONAL INFORMATION TO STUDY THE OLFACTORY BULB AND SUBSTANTIA NIGRA

In **Study IV**, due to head movements during both DTI series, 1 healthy individual and 4 PD patients were excluded. Thus, 15 healthy individuals (44–72 years, mean age 60, 9 men and 6 women) and 14 PD patients (47–73 years, mean age 64, 8 men and 6 women) were included. All 14 PD patients had a significant reduction of  $^{123}\text{I}$ -Ioflupane putaminal binding (quantified with BRASS software) and the mean asymmetry index was 12%. The 15 healthy individuals were normosmic or microsmic; 8 normosmic, 6 mild microsmic and 1 moderate microsmic. The 14 PD patients were anosmic or hyposmic; 7 were anosmic, 4 severe microsmic and 3 moderate microsmic. Hoehn & Yahr scores ranged between 1.5 and 2.0, and total Unified Parkinson Disease Rating Scale scores between 24 and 43. There was a significant difference ( $p < 0.001$ ), with minimal overlap, in the UPSIT scores between healthy individuals and PD patients.

In the first DTI series 13 healthy individuals and 13 PD patients (7 men and 6 women in each group; healthy individuals mean age 60 and PD mean age 64;  $p = 0.24$ ) were included, and in the second 11 healthy individuals (7 men and 4 women) and 8 PD patients (5 men and 3 women) were included (healthy

individuals mean age 61 and PD mean age 67;  $p=0.11$ ). Of the excluded single DTI series, 1 was due to technical problems and 12 due to head movements.

In all included 29 individuals the mean OB transaxial diameter was 3.0 (minimum=2.0 mm) and mean length 11.1 mm (minimum=9.0). For the healthy individuals group, mean OB volumes for the selected OBs were 47 mm<sup>3</sup> and 45 mm<sup>3</sup> for the first and second series, respectively, while it was 53 mm<sup>3</sup> and 52 mm<sup>3</sup>, respectively, for the PD group. The mean OB volumes for the selected OBs did not differ between groups for neither series ( $p=0.14$ ,  $p=0.19$ ).

In healthy individuals mean FA for the selected OBs was for the first and second series 0.22 and 0.20, respectively, while it was for PD patients 0.16 and 0.18, respectively. For healthy individuals mean MD for the selected OBs was for the first and second series  $1.5 \times 10^{-3}$  mm<sup>2</sup>/s and  $1.4 \times 10^{-3}$  mm<sup>2</sup>/s, respectively, while it was for PD  $1.7 \times 10^{-3}$  mm<sup>2</sup>/s and  $1.5 \times 10^{-3}$  mm<sup>2</sup>/s, respectively. CV for mean FA was 15% and for mean MD 11%. Measurements showed significant differences for the selected OBs between healthy individuals and PD patients in the first series, both on FA ( $p<0.001$ ) and MD ( $p<0.01$ ), but not in the second series, neither for FA ( $p=0.36$ ) or MD ( $p=0.58$ ).

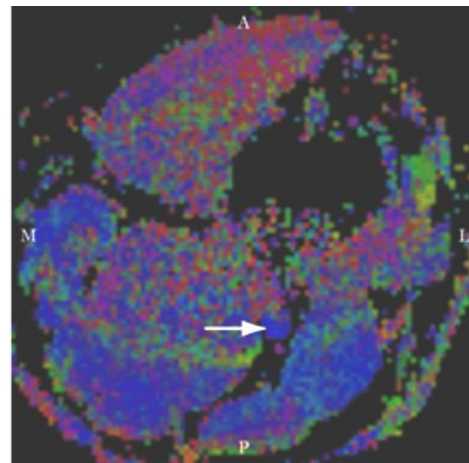
For healthy individuals mean FA for SN was for the first and second series 0.41 and 0.40, respectively, while it was for PD patients 0.37 and 0.36, respectively. Measurements showed significant differences for SN in both series on FA ( $p<0.01$ ,  $p<0.05$ ). For healthy individuals mean MD was for the first and second series  $0.79 \times 10^{-3}$  mm<sup>2</sup>/s and  $0.77 \times 10^{-3}$  mm<sup>2</sup>/s, respectively, while it was for PD patients  $0.82 \times 10^{-3}$  mm<sup>2</sup>/s and  $0.80 \times 10^{-3}$  mm<sup>2</sup>/s, respectively. No significant differences were seen in MD on neither series ( $p=0.50$ ,  $p=0.30$ ). CV for both mean FA and mean MD was 5%.

For healthy individuals mean FA for CC was for the first and second series 0.66 and 0.64, respectively, while it was for PD patients 0.65 and 0.64, respectively. For healthy individuals mean MD was for the first and second series  $0.85 \times 10^{-3}$  mm<sup>2</sup>/s and  $0.87 \times 10^{-3}$  mm<sup>2</sup>/s, respectively, while it was for PD patients  $0.87 \times 10^{-3}$  mm<sup>2</sup>/s and  $0.87 \times 10^{-3}$  mm<sup>2</sup>/s, respectively. Measurements showed no significant differences for CC between healthy individuals and PD patients in both series for FA ( $p=0.33$ ,  $p=0.77$ ) and MD ( $p=0.07$ ,  $p=0.83$ ). CV for mean FA was 3% and for mean MD 2%.

## 4.5 THE ‘HUDDINGE SPINOCEREBELLAR ATAXIA FAMILY’ – MRI ANALYSIS OF BRAIN, SPINAL CORD AND PERIPHERAL NERVE

In **Study V** of a peripheral nerve, one patient (#2) was excluded since the distal thigh was too bulky to fit into the coil, due to a high amount of subcutaneous tissue. One patient (#3) had its division of the sciatic nerve, into the common peroneal and tibial nerve, proximal on the thigh and therefore the broader tibial nerve was examined. In the other two participants the sciatic nerve was examined. In all three studied patients maximum FA was lower than for the healthy controls, which was significant ( $p < 0.01$ ) (Figure 21, Table 2).

Figure 21. An axial FA image of the left thigh in a patient of the Swedish 'Huddinge SCA Family' with an arrow indicating the sciatic nerve. A: Anterior; M: Medial; L: Lateral; P: Posterior.



	SCA	Control	SARA correlation
mesencephalon	0.33±0.01%	0.35±0.03%	0,22
pons	1.20±0.13%	1.58±0.12%	-0,68
medulla oblongata	0.35±0.05%	0.50±0.04%	-0,75
cerebellum	9.25±0.68%	11.48±0.47%	-0,62
spinal cord	5.5±0.4 mm	6.7±0.3 mm	-0,69
peripheral nerve max FA	0.45±0.01	0.57±0.04	-0,97
peripheral nerve MTR	14±7%	18±3%	0,25
muscle MTR	39±1%	40±1%	

Table 2. Data for the SCA group and control group. MRI volumetry showing the percentage of total brain volume for mesencephalon, pons, medulla oblongata and cerebellum. Mean midsagittal diameter for the spinal cord. Maximum FA and MTR for a peripheral nerve. MTR for muscles. Correlation of patient MRI measurements with SARA scores.

No significant difference ( $p=0.36$ ) was seen in mean MTR between the three patients and the healthy controls (Table 2). For comparison, MTR was calculated for the vastus medius muscles. No significant difference ( $p=0.22$ ) was seen in mean muscle MTR between the three patients and the healthy controls (Table 2).

### 4.5.1 Clinical details, ENeG, brain and spinal cord volume alterations

In **Study V** all patients had clinical signs of cerebellar ataxia, symmetric PNP, areflexia/severe hyporeflexia, dysautonomia symptoms (varying degree of orthostatism, syncope and erectile dysfunction) and dysarthria. None of the patients had reduced visual acuity, behaviour disturbances, cognitive decline, deafness or extrapyramidal symptoms (i.e. bradykinesia, resting tremor, dystonia or involuntary movements). SARA scores are presented in Table 1. All controls were normal on neurological investigation.

ENeG showed that:

Patient#1 had a normal motor conduction of the *right* tibial nerve, but no registration was found in the *right* sural nerve. These findings are compatible with axonal sensory neuropathy.

Patient#2 had a somewhat low amplitude distal muscle response on stimulation and slightly decreased motor conduction speed of the *left* tibial nerve. No registration was found in the *left* sural nerve. These findings are compatible with a sensorimotor neuropathy, which is predominately axonal and somewhat more pronounced for sensory nerve function.

Patient#3 (index case) had a somewhat low motor conduction speed, highly decreased distal latency, highly decreased response amplitude and F-response with delayed latency of the *right* tibial nerve. These findings are compatible with a moderate motor neuropathy, most probably axonal neuropathy.

Patient#4 had a normal motor conduction of the *right* tibial nerve. Normal conduction speed with very low amplitude response was found in the *right* sural nerve. These findings are compatible with axonal sensory neuropathy.

A sural nerve biopsy in patient#1 showed moderate loss of myelinated fibers, both of large and small fibers. No inflammatory cells were found.

MRI volumetry showed in all patients that pons, medulla oblongata, and cerebellum were significantly smaller ( $p<0.005$ ,  $p<0.01$ ,  $p<0.005$ ) in percentage of total brain, than in the healthy controls (Table 2, Figure 22). For mesencephalon there was no significant difference ( $p=0.15$ , Table 2), although the trend was a smaller mesencephalon in patients compared with healthy controls (three patients had a smaller mesencephalon). As a consequence of a smaller pons, medulla oblongata and cerebellum, and normalisation to total brain volume, the cerebrum was significantly ( $p<0.005$ ) larger in the patients. No significant difference ( $p=0.87$ ) was seen in total brain volume. In all patients the mean midsagittal spinal cord diameter was significantly smaller ( $p<0.05$ ) than in the healthy controls (Table 2, Figure 23).

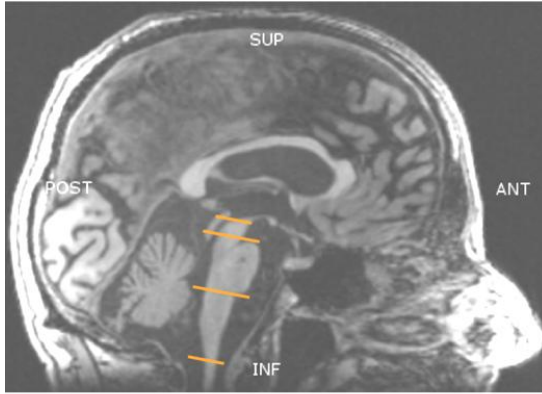


Figure 22. A sagittal T1-weighted brain image in a patient of the Swedish 'Huddinge SCA Family'. Segmentation of mesencephalon, pons and medulla oblongata is illustrated with lines. SUP: Superior; POST: Posterior; ANT: Anterior; INF: Inferior.



Figure 23. A sagittal T2-weighted upper spinal cord image in a patient of the Swedish 'Huddinge SCA Family'. SUP: Superior; POST: Posterior; ANT: Anterior; INF: Inferior.

Conventional MRI of the brain showed no infarcts, haemorrhages or tumours. Minor degenerative periventricular white matter changes were seen in one patient (#3) and one control (#1). One control (#4) had a small pineal cyst. The pons was evaluated for the 'hot cross bun' sign<sup>66</sup>, which none of the participants had. No focal changes were seen in the spinal cord. In one patient (#1) fat atrophy was noted in the semimembranosus and biceps femoris longus muscles.

Correlations of SARA scores with MRI measurements are shown in Table 2. There was a high negative correlation of SARA scores with the volume of pons, medulla oblongata, cerebellum and maximum FA of a peripheral nerve.

## 5. DISCUSSION

### 5.1 NERVE DIFFUSION TENSOR IMAGING

#### Study I

Study I was the first published study (2004) to show that human peripheral nerves, sciatic nerves, could be visualised *in vivo* using DTI and fiber tracking, despite the diffusion technique's inherent difficulties with low SNR, sensitivity to patient motion, field inhomogeneities and fast T2 relaxation.

DWI and DTI are techniques suffering from a low SNR and low spatial resolution<sup>16,17</sup>. Due to the faster T2 relaxation (surrounding muscles) and consequently a lower SNR<sup>67</sup>, PNS can be more difficult to image than the CNS. According to Eq. [4], a higher b-value will produce more echo attenuation, thus lower SNR<sup>68</sup>. However, decreasing the b-value to increase SNR will decrease the amount of diffusion-weighting<sup>69</sup>. For SNR reasons a b-value of 400 s/mm<sup>2</sup>, i.e. in the lower range, was chosen in **Study I**. Since the signal intensity is proportional to the voxel volume<sup>70</sup>, the peripheral nerve with the largest transaxial diameter, the sciatic nerve, was examined and the voxel size was 2.5×2.5×6.0 mm. Subsequent studies examining the median nerve, have for fiber tracking established an optimal b-value of 1025 s/mm<sup>2</sup> at 1.5 T<sup>69</sup> and between 1000-1400 s/mm<sup>2</sup> at 3 T<sup>71</sup>. There is no general agreement on what b-value to use for brain imaging, although a similar b-value of 1000 s/mm<sup>2</sup> is recommended<sup>14,15,72</sup>. However, and important, comparing studies with different b-values is problematic since the trace, MD and FA all depend on the b-value<sup>72,73</sup>. To estimate the tensor in DTI, at least six non-collinear diffusion-encoding directions and one without diffusion-weighting, or a very low b-value, is needed<sup>15</sup>. To further improve SNR, NSA can be increased or extra diffusion-encoding gradient directions used. Doubling NSA or gradient directions will have the same effect on the scanning time<sup>15,74</sup>. In **Study I** 32 diffusion-encoding directions were used. According to a simulation study, a minimum of 30 directions is recommended for a good tensor orientation estimation<sup>15</sup>. As long as the diffusion directions are well balanced, comparing studies with different diffusion-encoding gradient schemes is feasible<sup>74</sup>.

A single-shot diffusion-weighted EPI sequence was used in **Study I**, due to its fastness and simplicity, although other sequences can be used, e.g. a multi-shot diffusion-weighted EPI sequence<sup>68</sup>. Since the entire k-space is filled in one instance, the single-shot EPI sequence is relatively insensitive to patient motion, which is more problematic outside the CNS<sup>15,67</sup>. However, the limitations are many, e.g. a low spatial resolution due to T2\* relaxation during the acquisition. It is also sensitive to magnetic field inhomogeneities, chemical shift and susceptibility effects (off-resonance effects) due to a narrow bandwidth in the phase-encoding direction. Finally, there are geometric distortions due to susceptibility effects and eddy currents<sup>15,68,75</sup>.

The bipolar diffusion-encoding gradients have a high magnitude and long duration, which results in eddy currents. Eddy currents will result in residual small gradient fields interfering with the read-out gradient and thereby causing spatial distortion. If the eddy current effects are not cancelled or reduced, they will result in considerable image distortion. These artifacts can be reduced with a twice-refocused spin echo pulse, instead of the conventional diffusion pulse<sup>76</sup>. This pulse is vendor-dependent and was not available on the Philips MR-scanner in **Study I**, **II**, **III** and **IV**, but available on the Siemens MR-scanner and was used in **Study V**. If the twice-refocused spin echo pulse is used or not, can contribute to a variation in diffusion data when comparing between different MR-scanners<sup>77</sup>. The twice-refocused spin echo pulse may slightly increase TE and reduce SNR<sup>15,75</sup>.

Several methods exist to visualise DTI data<sup>78</sup>. One method is fiber tracking, which is a 3-dimensional method using algorithms to construct ‘fibers’ and has been validated in human post-mortem tissue<sup>29,79</sup>. Isotropic voxels are preferable, although not necessary<sup>33,80</sup>. It uses tensor anisotropy information, i.e. FA and tensor orientation characteristics, to construct fibers. A starting point, i.e. a seed point, is selected and a propagation line (the fiber) is created if the defined criteria for iterative propagation are fulfilled, i.e. the largest fiber deviation, minimum fiber length, step size and anisotropy threshold<sup>29</sup>. All these criteria are user-selected and will affect the end result<sup>80</sup>, which will also be affected by noise and the seed point size<sup>81</sup>. With these iterative propagation techniques, noise errors accumulate as the propagation becomes longer<sup>82</sup>. Even the location of the seed point within a voxel can significantly affect the end result. Multiple ROIs can be selected with the criterion that fibers have to pass through them<sup>80</sup>, which was used in **Study I**. The vast different algorithms available will also affect the result<sup>30,80</sup>. However, one study analysing the median nerve<sup>83</sup>, showed moderate to substantial correlation between two software packages. Altogether, this makes quantitative measurement with fiber tracking difficult. In brain fiber tracking the variability can be reduced by increasing the diffusion-encoding directions from 15 to 30, and accuracy can be improved by increasing NSA from 1 to 2<sup>84</sup>.

## Study II

**Study II** showed that peripheral nerves, sciatic nerves including their division into the tibial and common fibular nerves, have a characteristic diffusion pattern. This allowed nerves, excluding other tissues and artifacts, to be visualised using a novel approach called DDI and also with a simple unidirectional diffusion MIP approach.

A limiting factor in the tensor model is that the largest eigenvector, i.e. the nerve fiber direction, is in the direction of the largest signal attenuation and thereby most sensitive to a low SNR<sup>19,21</sup>. In **Study II** the diffusion-encoding gradient



directions were designed as a fan, and as expected the least signal attenuation was perpendicular to the nerve direction (Figure 15 and 24).

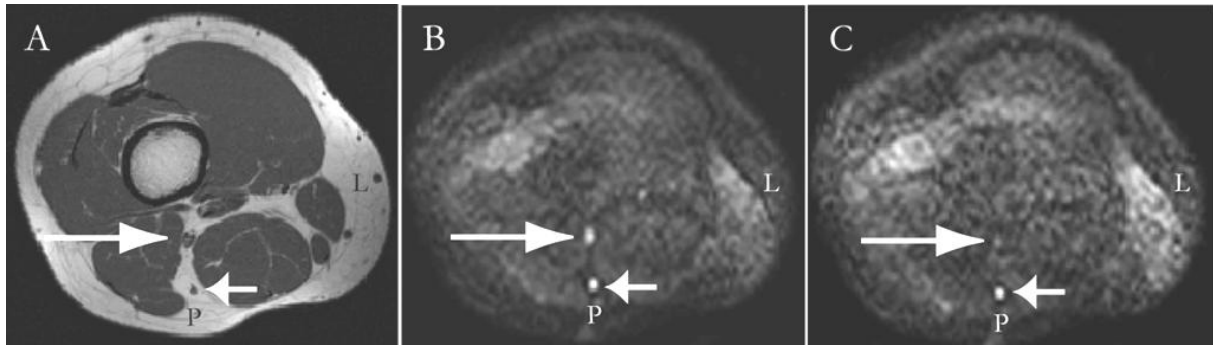


Figure 24. The long arrow indicates the sciatic nerve in an axial slice. The short arrow indicates a vessel. A) T1-weighted anatomical reference. B) DWI with diffusion-encoding direction perpendicular to nerve (direction 18). C) DWI with diffusion-encoding direction parallel to nerve (direction 36). L: Left; P: Posterior.

This information was used for nerve visualisation by using a simple unidirectional diffusion MIP approach (Figure 19A, B). The use of unidirectional diffusion MIP has subsequently been found feasible in studies evaluating the sacral plexus and peripheral nerves<sup>85,86</sup>. In a post-processing technique called ‘soap-bubble MIP’, user-defined curved ROI volumes were used to delineate the sacral plexus from surrounding tissues, e.g. the bone marrow and lymph nodes<sup>85</sup>.

By using DDI it is possible, without manual ROI techniques, to image the nerves, while suppressing other tissues as vessels, artifacts and muscles (Figure 19C). In **Study II**, a high b-value of 1000 s/mm<sup>2</sup> also contributed to suppressing muscle, which is used in ‘diffusion-weighted whole body imaging with background body signal suppression’<sup>87</sup>. The diffusion curves do not entirely reflect diffusion, since there is an exponential decay of the MR signal. However, due to the simplicity of the post-processing method in DDI, this was not compensated for when separating perpendicular diffusion from parallel diffusion in the nerves.

SENSE, a parallel imaging technique<sup>88</sup>, was used in **Study II**. Phase-encoding is time consuming and with parallel imaging fewer lines in k-space can be collected. The distance between the phase-encoding lines is increased, while the spatial resolution is kept the same. This introduces aliasing, which can be removed by using the phased-array coils varying spatial sensitivities. The acquisition speed is increased by an acceleration factor, e.g. a factor of two shortens the time by the same factor, since half of the phase-encoding lines in k-space are sampled<sup>88</sup>. The acceleration factor can as a maximum assume the number of elements used in the phased-array coil, although acceleration factors between 1.5 and 3 are normally used<sup>15,88</sup>. In images acquired with parallel imaging techniques, noise is located more in the image center than in the periphery, clearly more evident in higher accelerated

images<sup>88,89</sup>. Parallel imaging reduces susceptibility artifacts by increasing the phase-encoding speed in k-space<sup>90</sup>, reduces image blurring<sup>68</sup> by filling the outer k-space with higher SNR where the details are collected and increases SNR by reducing TE<sup>17,91</sup>. Best SNR efficiency for an eight-element head coil was reported with a b-value of 1000 s/mm<sup>2</sup>, an acceleration factor of 2.1 and partial Fourier encoding of 60%<sup>17</sup>. An additional study has reported an acceleration factor of 2 as better than acceleration factors zero, 3 or 4, both quantitatively and qualitatively<sup>92</sup>.

Reducing pulsation artifacts with cardiac gating has been proposed<sup>12</sup>, although this was not used in **Study II**, since it would have prolonged an already long sequence. Regional saturation technique (REST) has been used in peripheral nerve DTI studies to minimise flow artifacts<sup>93</sup>. REST is a saturation band, which at its location applies a 90° RF pulse directly prior to the imaging sequence RF pulse<sup>70</sup>. REST slightly prolongs TR and it was tested in one individual. There was no obvious improvement and was not used in **Study II**, although it was not thoroughly exploited (Figure 25).

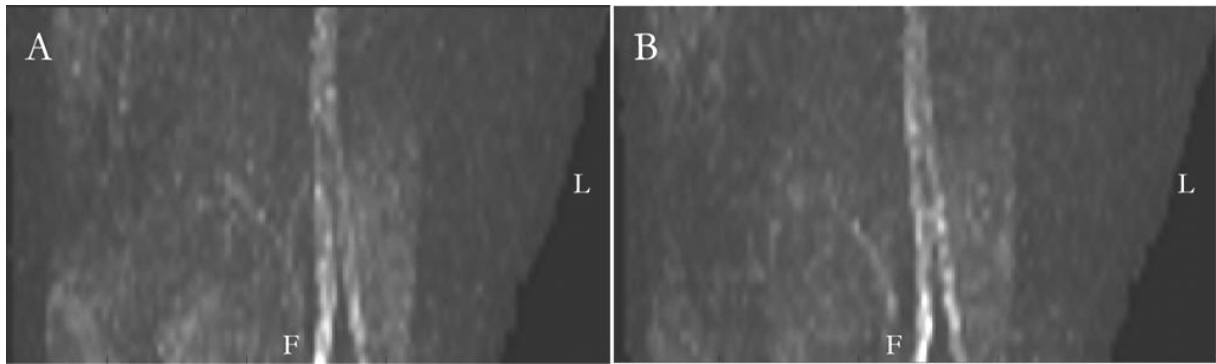


Figure 25. Coronal view of DDI images without (A), and with regional saturation technique (REST) (B). L: Left; F: Feet.

## Study III

Study III was the first published study to show that OB and olfactory tracts could be visualised *in vivo* using DTI and fiber tracking, despite localised in an area prone to susceptibility artifacts.

OBs and olfactory tracts are anatomically close to air-filled sinuses and bone, and therefore exposed to susceptibility artifacts<sup>7,94</sup>. The direction of these artifacts depends on the phase-encoding direction. In conventional EPI sequences, k-space is sampled with a rectangular/Cartesian approach. K-space is traversed from top to bottom or the reverse (Figure 9), thus with positive or negative phase-encoding blips<sup>75,91</sup>. By employing the phase-encoding direction anterior-posterior (‘fold-over direction’; Philips) and using negative phase-encoding blips (‘fat-shift direction anterior’; Philips) artifacts were displaced posterior and not at the location of the OBs (Figure 26A), which was used in **Study III** and **IV**.

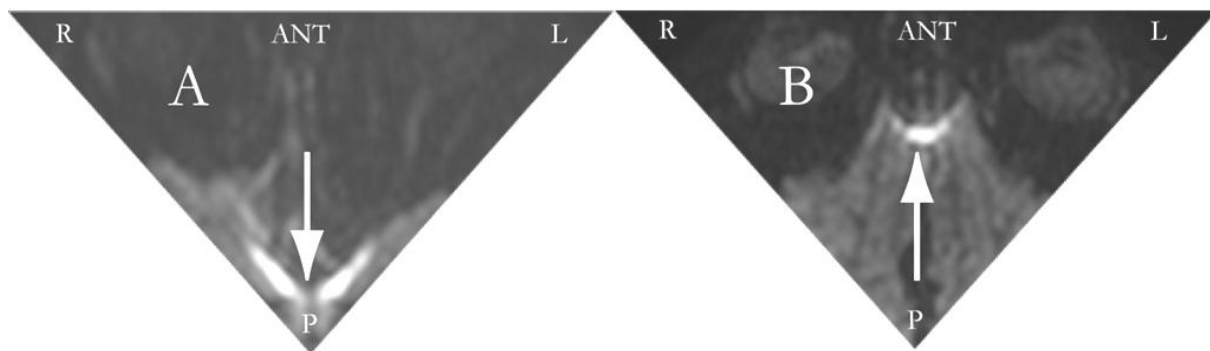


Figure 26. Arrow pointing at an artifact displaced posterior (A) and anterior (B). R: Right; ANT: Anterior; L: Left; P: Posterior.

With positive phase-encoding blips, the OBs were obscured by the artifacts (Figure 26B). In functional MRI it is also important, depending on the area of interest, to traverse k-space in different directions<sup>95</sup>. To reduce geometric distortion there are techniques that would be of interest to exploit in this location, e.g. acquiring and combining k-space in reverse directions or measuring the b-zero field for a retrospective correction<sup>33,72</sup>.

The MR signal is continuous, but sampled in a discrete manner. According to the Nyquist theorem, the minimum sampling that is needed to correctly display the frequency are two equally spaced samples acquired within one cycle of the highest frequency component<sup>70</sup>. The receiver bandwidth is the range of the sampling frequency and is inversely proportional to the sampling interval, thus doubling the sampling interval will reduce the receiver bandwidth by half. Consequently, it will be narrower, but with a longer sampling time and longer TE<sup>96</sup>. If the sampling rate is fixed and the frequencies are lower, the time has to be prolonged in order to sample enough according to the Nyquist theorem. Noise is random and distributed uniformly over the whole bandwidth, and since a narrow receiver bandwidth does not sample high frequencies, this will result in a higher SNR. Noise is proportional to the square root of the bandwidth, albeit with a narrow receiver bandwidth the minimum TE can be longer, which also affects SNR<sup>70</sup>. Artifacts will be displaced for a longer distance with a narrow receiver bandwidth. Thus, a receiver bandwidth of 1000 Hz and 10 pixels in one direction will yield 100 Hz/pixel, while a wider receiver bandwidth of 10000 Hz and again 10 pixels in one direction will result in 1000 Hz/pixel. A wide receiver bandwidth ('water-fat-shift minimum'; Philips) was used since k-space is traversed faster, i.e. shorting the sampling time, which results in less distortion. In single-shot EPI the sampling interval is long in the phase-encoding direction, consequently the bandwidth is narrow. Small frequency differences due to inadequate shimming, chemical shift and susceptibilities will therefore have large displacement in this direction, i.e. large image distortion effects<sup>91</sup>.

Eddy-currents also contribute to artifacts. Even if eddy-current correction is used to lessen the effect and artifacts are displaced from the area investigated, the misregistration artifacts still contribute to all voxels in the acquired data<sup>72</sup>. Different techniques exist to traverse the phase-encoding direction faster, which would reduce the artifacts, and are of interest to explore in this anatomical location, e.g. PROPELLER, Propeller EPI in the other direction and read-out segmented EPI<sup>75,97-99</sup>. The PROPELLER technique utilises oversampling of central k-space for self-navigation, i.e. motion correction, which will cause longer scanning times<sup>15</sup>. Multi-shot imaging is somewhat problematic in DTI, since all of the k-space is not acquired at the same time. Any minimal motion between the shots introduces artifacts and single-shot techniques are currently predominant<sup>91</sup>.

Eddy current distortions are seen as three types of geometric distortion; scaling, translation and shear<sup>11,72</sup>. Eddy current distortions and simple motion can to some extent be corrected with post-processing. There are several different software programs and vendor-specific algorithms available. FSL provides an affine registration using 12 degrees of freedom, aligning each slice's diffusion-weighted images to its reference image/b-zero, regardless of eddy current artifacts or patient motion. This was used in **Study III** and **IV** (<http://www.fmrib.ox.ac.uk/fsl>). However, correcting for large motion is harder, and motion occurring in the z-axis is not corrected for, since the reference image could partially or fully be a different b-zero. The strong diffusion-encoding gradients also cause low-frequency mechanical resonance vibrations of the patient table, contributing to motion artifacts<sup>100</sup>. Measuring motion can be complicated, especially since there often is during long examinations a small anatomical drift summarised to a larger distance<sup>101</sup>, albeit new motion correction techniques are evolving. One study used a camera to optically analyse head movement<sup>102</sup> and another study utilised a retrospective approach for image reconstruction<sup>103</sup>. The issue of motion is often neglected in published clinical papers, and during the lengthy DTI sequence in **Study IV** there was a considerable exclusion owing to motion. Due to head movement during an acquisition, there is in ROI analyses a positive bias in MD, and just removing images with large artifacts is insufficient<sup>104</sup>. Prior to post-processing in **Study IV**, the diffusion-weighted images were visually analysed for head movements in three reconstructed planes. B-matrix reorientation was performed after eddy current/motion correction<sup>101</sup>. Theoretically this should be performed on data after an affine registration using 6 degrees of freedom, i.e. only motion, since eddy currents effects are random. B-matrix reorientation was still used. However, participant motion was excluded visually and the reorientation effect was thereby minor.

The OBs are small and the reconstructed voxel size in **Study III** and **IV** was  $0.9 \times 0.9 \times 3.0$  mm. SNR is important in DWI and DTI<sup>16</sup>, and  $\text{SNR} \propto \sqrt{\text{NSA}}$ <sup>96</sup>. The small voxels will decrease SNR and as compensation, four NSA was used and the

b-value was slightly shortened, 900 s/mm<sup>2</sup> as compared to 1000 s/mm<sup>2</sup> for standard brain protocols<sup>14,15</sup>. Although 3.0 T MR-scanners provide more SNR than 1.5 T, the susceptibility artifacts are more severe due to the faster T2\* relaxation<sup>15,35,105</sup>. To reduce geometric warping, i.e. artifacts from off-resonant spins or susceptibility artifacts, TE should be kept short<sup>15,68,105</sup>. This can be achieved by using maximum diffusion-encoding gradient strength/slew rate, ramped sampling, parallel imaging and partial Fourier encoding<sup>17,92,96</sup>. Higher resolution, i.e. smaller voxels, will reduce susceptibility artifacts<sup>70</sup>. Reporting SNR in studies could be considered<sup>89</sup>. SNR can be measured in several ways, the simplest is using a ROI in the acquired image, e.g. measuring the mean signal intensity in the mean diffusion-weighted image (i.e. all diffusion encoded directions) or in the mean b-zero image, divided by the SD of the noise in the image background<sup>89</sup>, sometimes using a correction factor<sup>69</sup>. One b-zero (or low b-value) image for every 5-10 diffusion-weighted image is considered optimal<sup>106,107</sup>, which was not possible with the MR-scanners<sup>15</sup> used in **Study I-V**. In ‘high-FA’ regions (approximately FA 0.80) a SNR of 20 is recommended, in ‘medium-FA’ (approximately FA 0.45) a SNR of 40, and in ‘low-FA’ regions (approximately FA<0.20) SNR 50 at 1.5 T and SNR 70 at 3.0 T<sup>33,89</sup>. Two studies of the median nerves<sup>69,108</sup>, using a b-value of 1025 s/mm<sup>2</sup>, reported a SNR of 56 and 59 at 1.5 T. A low SNR can cause a bias in FA, which can vary with different factors, e.g. what region of the brain is examined, head size, hardware and software<sup>33,89,109</sup>. With a low SNR an upward FA bias is seen<sup>110</sup>. Changing the number of diffusion-encoding gradient directions, NSA or voxel size, and thereby affecting the SNR, can cause intra-individual FA differences<sup>111</sup>.

Fiber tracking was used in **Study III** to visualise OBs and olfactory tracts. The proximal portion of the olfactory tracts could rarely be fiber tracked, since the tracts split up into fibers with very thin diameters, compared to the DWI axial slice diameter. As a negative control a patient with congenital anosmia was examined, where neither OBs nor olfactory tracts were seen on T2-weighted nor the fiber tracking images. For fiber tracking, FA threshold was 0.18 in **Study III**, similar to previous fiber tracking studies of other cranial nerves<sup>112,113</sup>.

## Study IV

Using a novel approach for more objective ROI placement, altered diffusion was found in OBs in the PD group, as compared to healthy individuals. However, the intra-individual variability was high, due to OBs small size and location susceptible to artifacts, and the difference between the groups was significant only for the first of two series.

OBs are small and therefore a time-consuming high spatial resolution MRI sequence was used. Since OBs are located in a region susceptible to artifacts, the intra-individual variability was tested by performing two identical DTI sequences and CV was calculated. Prior to eddy current/motion correction, diffusion-weighted images were visually analysed for head movements in three reconstructed

planes. Several participants had to be excluded due to head movements, since even a small head movement would affect the measurements. Hyposmia is noted early in PD<sup>9</sup> and olfaction impairment was clearly evident in the 14 PD patients included (and the 4 excluded) in **Study IV**. OB volume was measured, since smaller OB volumes would result in more partial volume effects, which could otherwise falsely explain a diffusion difference. No difference was found between PD patients and healthy individuals for the selected OBs. Another study<sup>53</sup> similarly found that the OB volume was not different in PD patients compared to healthy controls. The measures of the OBs' transaxial diameters and lengths in **Study IV** were similar to reported data<sup>8</sup>. At a b-value of 1000 s/mm<sup>2</sup>, white and grey matter have similar trace, despite a high difference in FA<sup>72</sup>. Contribution of cerebrospinal fluid will increase MD (trace/3). MD was similar in SN and CC, while increased MD was seen in OB, due to the partial volume effect of cerebrospinal fluid.

Even if DTI is corrected for eddy currents and minor motion, small anatomical residual distortions still remain. Due to the diffusion technique's local misalignment artifacts, it is suboptimal for ROI placement to solely depend on a non-diffusion anatomical sequences and even a b-zero image<sup>72</sup>. The OB's small size and location susceptible to artifacts cause a high user-dependent ROI placement variability, making DTI measurements in these regions challenging. Since the left and right OBs often are situated slightly different in the superior-inferior axis (Figure 16A), both were not to an equal extent included in the axial 3 mm DTI slice. For example, if one OB is divided between two axial slices, using a regular ROI anatomical placement technique, it would actually measure the diffusion in two consecutive axial slices, i.e. in a 6 mm superior-inferior axis. Given these difficulties, a novel approach in which ROI placement not only relies on anatomical data but also on the inherent diffusion directional information in DTI was used. Each ROI was placed in only one slice in the location of each OB, in which the diffusion was highest in an anterior-posterior axis correlating to their anatomical direction. Due to partial volume effects, only the ROI with the smallest  $\alpha_y$  angle was used for analysis in each individual, since the side with higher  $\alpha_y$  angle is not likely to fully represent the OB. Tilting of the axial diffusion slices in a left-right plane to cover both OB would have allowed comparison of left and right OB diffusion. However, this was not possible since the post-processing diffusion steps required non-tilted slices. In addition, would it have made placement of the SN ROIs more difficult. In the PD group, compared to healthy individuals, FA was decreased and MD increased in the OBs. However, the intra-individual variability was high in OBs, owing to their small size and location susceptible to artifacts, and the difference between the groups was significant only for the first of two series. Moreover, a low SNR could contribute<sup>89</sup>. In OB the CV was 11-15%, while it was in SN 5% and in CC 2-3%. Similar CVs have been reported, with smaller variations in major white matter and larger in grey matter<sup>114</sup>. Diffusion alterations were hypothesised, since  $\alpha$ -synuclein inclusions and Lewy neurites interfering with nerve structure have been detected in OBs<sup>9</sup>. Even though diffusion was only measured in

one of each patient's OBs, UPSIT showed highly significant olfaction impairment in the PD group and close to normal scores in the healthy individuals. Thus, the diffusion differences could therefore hardly be explained by a unilateral OB involvement. Similar alterations in FA and MD have also been found in a study on optic neuritis<sup>115</sup>. In a study using anatomical ROI placement, diffusion alterations were found in 'the anterior olfactory structures'<sup>116</sup> and in a study using voxel-wise group statistical analysis, diffusion alterations were found in the 'location of the olfactory tracts'<sup>49</sup>. In idiopathic REM sleep behaviour disorder, a risk marker for PD, a voxel-wise group statistical analysis found diffusion alterations in the 'olfactory region'<sup>117</sup>. Even though the diffusion alterations could not be reproduced in the second series, this could be due to a minimal difference in head position, which would produce other partial volume artifacts (Figure 16A). Another contributing factor could be the fewer participants in the second series, since the trend for mean FA and mean MD was similar to the first series. The second series comprising fewer participants could reflect the problem of remaining motionless for a prolonged time period.

In the two DTI series in **Study IV** the mean smallest  $\alpha_v$  angle in OBs was similar in the PD group and healthy individuals, indicating that although FA is decreased in PD patients, the tensor is still directed along the OBs. In late-stage PD, OBs can theoretically have  $\alpha$ -synuclein inclusions and Lewy neurites to the degree that FA is very low or the tensor is no longer aligned along the OB, and thereby not depicted by the approach used in **Study IV**. Since olfaction often is impaired prior to motor symptoms in PD, it would be of interest to use imaging of the OBs as a biomarker for early diagnosis<sup>44,45,116</sup>. It may turn out that diffusion changes in the OBs occur prior to olfaction impairment. Since the degree of hyposmia already is high in early-moderate PD, an imaging biomarker rather than a smell test, may be superior to monitor disease progression. Diffusion alterations have also in PD patients been demonstrated in white matter adjacent to central olfactory cortex, suggesting that changes in several brain regions underlie olfaction impairment in PD<sup>118</sup>. In functional MRI the inter-individual variation in activation of main olfactory areas is high and therefore hard to use as a diagnostic tool in the individual patient<sup>119</sup>. 3.0 T and 9.4 T *in vitro* conventional MRI studies of the OBs can identify lamination<sup>8</sup>, i.e. the cellular layers, which would be interesting to evaluate in PD.

## Study V

Using DTI to study SCA patients with ENeG confirmed PNP, a significant FA reduction was seen in peripheral nerves, compared to healthy controls.

Since the bandwidth in EPI is narrow in the phase-encoding direction, chemically shifted signals from fat will be displaced several pixels in the phase-encoding direction, causing artifacts. Fat suppression is therefore compulsory<sup>70</sup>.

**Study V** was performed at 3.0 T and at this higher field strength, fat suppression is more problematic. This is due to RF inhomogeneities, since the wavelength is reduced<sup>35,70,120</sup>. SPAIR, an adiabatic pulse, was used for fat suppression, since it is more robust than SPIR to RF inhomogeneities<sup>70</sup>. Additional fat suppression with REST was applied on subcutaneous tissue.

In EPI, Nyquist ghosting artifacts can be seen. EPI uses strong gradients and residual eddy currents in electrically conductive MR-scanner structures are common. The residual eddy currents can lead to mistiming of gradient amplitudes and temporal shifts in the read-out direction. Using Cartesian k-space sampling, this will result in small lateral shifts for the different directions, i.e. Nyquist ghosting artifacts in the phase-encoding direction. The artifacts resemble foldover artifacts<sup>91</sup>. To reduce Nyquist ghosting artifacts, a reference scan and shimming are performed<sup>70</sup>. Since SNR is important, a transmit/receive 15-channel knee coil with an inner diameter of 154 mm was used to examine the distal thigh in **Study V**. Due to the inner diameter, one of the patients could not be examined, since the distal left thigh could not fit into the coil. The other three patients were examined and all had a lower maximum FA in the nerves compared to the healthy controls. Although MRI was performed on the left sciatic nerve/tibial nerve and ENeG on the right tibial nerve, all patients had clinical signs of symmetric PNP and neuropathy was confirmed by ENeG. In one of the patients, fat atrophy was noted in the semimembranosus and biceps femoris longus muscles. These findings support neuropathy<sup>121</sup>, since these muscles are innervated via the tibial part of the sciatic nerve.

SARA is a validated rating scale for ataxias with a good inter-rater reliability<sup>60</sup>. In SCA1, 2, 3 and 6, SARA scores of ataxia symptoms have been found to correlate with MRI volumetry of the brainstem and cerebellum<sup>57</sup>. In **Study V** there was a high negative correlation of SARA scores with the volume of pons, medulla oblongata and cerebellum. The highest negative correlation was seen with maximum FA of a peripheral nerve. Nerve diffusion tensor imaging performed with high precision and accuracy could be a promising potential biomarker of PNP. In an *ex vivo* high-resolution DTI study on mice, FA was decreased in axonal degeneration of peripheral nerves and also correlated with the total number of regenerating axons<sup>122</sup>. In a study on experimental contusion injuries in rat sciatic nerves, FA correlated more with axon density and diameter, than with myelin density and thickness. In the same study, FA was found to correlate with changes in histology and function<sup>123</sup>. In SCA1 and SCA2, decreased FA has been found in the brain and correlated with clinical symptoms<sup>58,124</sup>.



There are several studies measuring FA in peripheral nerves, both on normal nerves and on nerves with pathology<sup>69,125-137</sup> (Table 3).

<sup>a</sup> FT	Study	<sup>b</sup> T	<sup>c</sup> b	Nerve		HI	P	HI/P
						Max. FA measured	Max. FA measured	
No	Kakuda <sup>125</sup> <i>et al</i>	3	1000	Tibial	Group median FA	0.53	<sup>d</sup> 0.40	10/10
No	Skorpil <i>et al</i> [Study V]	3	1000	Sciatic/tibial	-II-	<sup>e</sup> 0.57	<sup>f</sup> 0.45	3/4
No	Tanitime <sup>126</sup> <i>et al</i>	3	1000	Tibial	-II-	<sup>g</sup> 0.52	<sup>h</sup> 0.44	26/22
No	Hiltunen <sup>127</sup> <i>et al</i>	3	1000	Tibial (knee)	-II-	0.85	-	3/0
No	-II-	3	1000	Peroneal	-II-	0.79	-	3/0
No	-II-	3	1000	Tibial (ankle)	-II-	0.73	-	3/0
No	-II-	3	1000	Median	-II-	0.74	-	4/0
No	-II-	3	1000	Ulnar	-II-	0.67	-	4/0
No	-II-	3	1000	Radial	-II-	0.62	-	3/0
						Mean FA measured	Mean FA measured	
No	Tagliafico <sup>128</sup> <i>et al</i>	3	1000	C5-C8	Group median FA	0.33	-	40
						Mean FA measured	Mean FA measured	
No	Guggenberger <sup>129</sup> <i>et al</i>	3	1200	<sup>i</sup> median	Group mean FA	<sup>k</sup> 0.59	<sup>kl</sup> 0.53	45/15
No	-II-	3	1200	<sup>m</sup> median	-II-	<sup>k</sup> 0.54	<sup>kl</sup> 0.44	45/15
No	-II-	3	1200	<sup>n</sup> median	-II-	<sup>k</sup> 0.48	<sup>kl</sup> 0.42	45/15
Yes	Hiltunen <sup>130</sup> <i>et al</i>	3	1000	Median	-II-	<sup>o</sup> 0.48/ <sup>e</sup> 0.42	<sup>l</sup> 0.42	12/12
Yes	Kabacki <sup>131</sup> <i>et al</i>	3	1000	Median	-II-	0.71	<sup>l</sup> 0.43	20/2
No	-II-	3	1000	<sup>p</sup> Median	-II-	0.59	-	20/0
No	-II-	3	1000	<sup>r</sup> Median	-II-	0.72	-	20/0
No	-II-	3	1000	<sup>s</sup> Median	-II-	0.71	-	20/0
No	Jambawalikar <sup>132</sup> <i>et al</i>	3	1000	Ulnar	-II-	0.75	-	10/0
No	Yao <sup>133</sup> <i>et al</i>	3	600	<sup>t</sup> Median	-II-	0.70	-	13/0
Yes	van der Jagt <sup>134</sup> <i>et al</i>	3	800	L4-S3	-II-	0.26	-	10/0
Yes	Balbi <sup>135</sup> <i>et al</i>	1.5	900	L5 or S1	-II-	0.22	<sup>u</sup> 0.19	19/19
No	Vargas <sup>136</sup> <i>et al</i>	1.5	900	C5-C8	-II-	0.30	<sup>x</sup> 0.24	6/11
No	Andreisek <sup>69</sup> <i>et al</i>	1.5	1025	<sup>p</sup> Median	-II-	0.50	-	15/0
						Mean FA measured	Mean FA measured	
Yes	Khalil <sup>137</sup> <i>et al</i>	1.5	400	Median	Group median FA	<sup>e</sup> 0.59	<sup>l</sup> 0.53	13/13

**Table 3. FA values in peripheral nerves in different studies. Healthy individuals (HI) and patients (P).**

<sup>a</sup>Fiber tracking derived FA values. <sup>b</sup>Tesla. <sup>c</sup>b-value (s/mm<sup>2</sup>). <sup>d</sup>Chronic inflammatory demyelinating polyradiculoneuropathy. <sup>e</sup>Age-matched. <sup>f</sup>Spinocerebellar ataxia. <sup>g</sup>Age-corrected. <sup>h</sup>(17 Chronic inflammatory demyelinating polyradiculoneuropathy, 3 Charcot-Marie-Tooth disease, 1 Guillain-Barré syndrome, 1 Churg-Strauss syndrome). <sup>i</sup>DRU-level. <sup>k</sup>Both readers. <sup>l</sup>Carpal tunnel syndrome. <sup>m</sup>Pisiforme-level. <sup>n</sup>Hamatum-level. <sup>o</sup>Young controls. <sup>p</sup>Flexor retinaculum. <sup>r</sup>Wrist level. <sup>s</sup>Forearm level. <sup>t</sup>Within carpal tunnel. <sup>u</sup>Compressed root. <sup>x</sup>At level of pathology.

The reported measures differ between studies, FA-values are derived from fiber tracking results or ROI analyses, and either the maximum or mean nerve FA was reported (Table 3). Since peripheral nerves are small in diameter, there is a potential risk that a ROI includes other tissues, e.g. muscles and fat, which have lower FA than nerves<sup>14</sup>. Consequently, maximum FA is preferable compared to mean FA, which was measured in **Study V** and in other studies<sup>125-127</sup>. In the statistical comparisons between groups, either the median or mean FA was reported (Table 3). Two studies have only illustrated FA-values in tables<sup>93,138</sup>. According to the studies presented in Table 3, maximum FA range in healthy individuals was 0.52-0.85 and mean FA range was 0.22-0.75. FA values decrease with age and ADC increases<sup>126,129,131</sup>, although this was not found in one study<sup>133</sup>. A reduction of FA values with age has also been observed in the brain<sup>139</sup>. Histopathological studies

have shown age-related changes in peripheral nerves, i.e. degeneration of myelin sheaths, axon deletion, microtubule changes and increasing interstitium, which could be a cause of the age-related diffusion changes<sup>129</sup>. FA values also decrease with a smaller nerve size<sup>127</sup>. Two studies have shown that FA decreases distally in the median nerve<sup>129,131</sup>, while another study did not<sup>133</sup>. FA and ADC does not correlate with gender<sup>126,129,133</sup>, and no intra-individual side difference has been observed in median nerves at wrist level or nerves in forearms<sup>93,108,133</sup>.

A high inter-reader<sup>129</sup> and high inter- and intra-reader agreement<sup>137</sup> have been reported in studies conducted on median nerves. However, the variance in normative data of the median nerve differs between studies, with low variance in one study<sup>129</sup> and higher in other studies<sup>108,131,133</sup>. A low variance is necessary to implement DTI in the clinical setting and the technique is challenging due to several reasons, e.g. field homogeneities, gradients and SNR<sup>129,133</sup>. Internal control of the contralateral nerve could be helpful in data interpretation<sup>108,130</sup>. On repeated examination, three weeks apart, the reproducibility was high<sup>108</sup>. For nerve evaluation, quantitative DTI measurement is preferred to qualitative fiber tracking<sup>30,80-82,108</sup>, nevertheless studies on optimisation of fiber tracking of median nerves have been performed. At 3.0 T the recommended parameters are a b-value of 1000-1400 s/mm<sup>2</sup>, a minimum FA threshold of 0.2 and a maximum angulation of 10 degrees<sup>71</sup>. At 1.5 T<sup>69</sup> the recommended b-value is 1025 s/mm<sup>2</sup>.

In all studies presented in Table 3, FA was decreased in patients, except in one study on carpal tunnel syndrome<sup>130</sup>. Several studies have focused on carpal tunnel syndrome<sup>129-131</sup>, while another disease that has been investigated is chronic inflammatory demyelinating polyradiculoneuropathy<sup>125</sup>, which in another study included Charcot-Marie-Tooth disease, Guillain-Barré syndrome and Churg-Strauss syndrome<sup>126</sup>. In **Study V** SCA patients, with clinical signs of PNP and ENeG verified PNP, were examined. In the three studied patients, maximum FA for a peripheral nerve was significantly lower than for the healthy controls (Table 2). A sural nerve biopsy in one of the patients showed moderate loss of myelinated fibers, both large and small fibers, with no inflammatory cells. In sciatic neuropathy conventional MRI may be helpful<sup>140</sup> and DTI is a promising complement in peripheral neuropathy<sup>141</sup>. In the brachial plexus, FA has been evaluated at the level of compressing neoplasms, although no statistical difference was found compared to healthy individuals<sup>136</sup>. However, decreased FA has been seen in compressed lumbar nerve roots<sup>135</sup>. FA is lower in normal nerve roots<sup>134,135</sup> than in other nerves. Possible explanations could be that spinal root nerve endoneurium contains much less collagen and a partial volume effect<sup>134,135</sup>.

In **Study V**, the maximum FA was registered. As mentioned in a study by Kakuda<sup>125</sup> *et al* and suggested by Hiltunen<sup>130</sup> *et al* maximum FA is a better measure than mean FA. Since nerves are small and can be difficult to separate from surrounding tissues on FA-CEI, ROI analyses are thereby sensitive to partial

volume effects. Nerves are often in the vicinity of muscles, which in the thigh have a FA range of 0.27-0.38<sup>142</sup>. Due to the potential partial volume effects in the ROI analysis, mean ADC was not evaluated in **Study V**, but has been evaluated in other studies. Mean ADC range reported in nerves of healthy individuals was 0.71–1.27<sup>132</sup>, 0.71–1.56<sup>127</sup>, 0.81-1.03<sup>141</sup> and 1.34–1.81<sup>128</sup> (all values  $\times 10^{-3}$  mm<sup>2</sup>/s). In a study on patients with carpal tunnel syndrome, the mean ADC was significantly altered compared to healthy individuals, except in the elderly<sup>129</sup>. In another study on carpal tunnel syndrome, MD was measured with considerable overlap recorded compared to healthy individuals<sup>130</sup>. An increase in ADC or MD could reflect oedema or inflammation<sup>130</sup>. ADC maps are seldom used, due to the low contrast to surrounding tissues<sup>127</sup>. In chronic inflammatory demyelinating polyradiculoneuropathy, swelling of nerve roots with increased signal intensity on T2-weighted or short tau inversion recovery images can be seen<sup>141</sup>. In this condition, mean ADC was elevated and ranged 0.84-1.70  $\times 10^{-3}$  mm<sup>2</sup>/s in the brachial and lumbar plexus, with overlap in the lower ADC range<sup>141</sup>.

**M**agnetisation transfer imaging was evaluated in **Study V**. This is a technique that images the non-mobile water pool bound to macromolecules, e.g. myelin, which otherwise is not imaged<sup>36,37</sup>. Decreased MTR indicate a reduction of free water that exchanges magnetisation, which is a non-specific finding, but in white matter in multiple sclerosis it is related to axon damage and demyelination<sup>36,38</sup>. MTR is not only correlated to myelin content, but also to inflammation and oedema<sup>39</sup>. MTR has been used *in vivo* in human healthy nerves<sup>40,41</sup>, although no studies on peripheral nerve pathology have been published. In **Study V** only one patient had reduced MTR and no statistical significance was found between the groups. Although a sural nerve biopsy in one patient showed moderate loss of myelinated fibers, the amount of myelin loss might be too small for detection with MTR.

## 5.2 CLINICAL IMPLICATIONS

**S**tudy IV showed that nerve diffusion tensor imaging could detect diffusion alterations in OBs in PD patients as a group, albeit the intra-individual variability was high.

**S**tudy V showed that nerve diffusion tensor imaging could, in SCA patients with PNP, detect diffusion alterations in peripheral nerves.

### 5.2.1 Other published studies

**S**everal studies have evaluated DTI in carpal tunnel syndrome<sup>129,130,137</sup> and a moderate/minor correlation of FA and ADC with ENeG was found<sup>143</sup>. Other

studies have investigated chronic inflammatory demyelinating polyradiculoneuropathy, Charcot-Marie-Tooth disease, Guillain-Barré syndrome G-B, Churg-Strauss syndrome<sup>125,126,141</sup>, compression from neoplasms or disc herniations<sup>135,136</sup>, median nerve repair<sup>144</sup>, optic nerves<sup>115,145</sup> and assessed axonal regeneration in animal peripheral nerves<sup>122,123,146</sup>.

### 5.3 NERVE DIFFUSION TENSOR IMAGING CONSIDERATIONS

#### ***M<sub>R-scanner</sub> – B<sub>0</sub>***

Scanning at higher Tesla results in higher SNR, albeit there are more susceptibility artifacts<sup>14,15</sup>. A homogenous B<sub>0</sub> within the voxel is a necessity. Since the human body itself will alter B<sub>0</sub>, shimming has to be performed. To reduce Nyquist ghosting artifacts, a reference scan and shimming are performed. The imaged body part of interest is best positioned as close to the center of the magnet as possible, where the most homogenous magnet field exists<sup>70</sup>.

#### ***R<sub>F-pulse</sub> – B<sub>1</sub>***

At higher field strengths, fat suppression is more problematic due to RF inhomogeneities<sup>70,120</sup>. A small FOV excitation using parallel RF transmission would improve the spatial resolution<sup>147</sup>. Transmitter coils can have less uniform B<sub>1</sub>, compared to the body coil (bore)<sup>70</sup>.

#### ***Coils***

It is often better to use smaller coils, since the largest noise contribution generally is from the patient. Array coils are used for parallel imaging. Receiver coils have to be positioned 90° against B<sub>0</sub> to detect the signal. Prescan is performed to characterise and optimise the transmitter and receiver coils<sup>70</sup>. Calibration of the gradient coils is part of a quality assurance program<sup>33</sup>.

#### ***G<sub>radient strength, Slew rate</sub>***

Gradient coils with high strength, ramped sampling and slew rate will result in shorter TE (Eq. [5]) and higher SNR<sup>15,68,96,105</sup>.

#### ***P<sub>atient motion</sub>***

Cardiac gating could be considered to reduce pulsation artifacts<sup>12</sup>. Measuring motion can be complicated, especially since there often is a small anatomical drift that can add up to a considerable distance during long examinations<sup>101</sup>. However, new techniques are currently developed, e.g. using a retrospective approach for image reconstruction or a camera for motion correction<sup>102,103</sup>.

#### ***S<sub>NR-check</sub>***

Reporting the SNR in studies could be considered, since a low SNR can cause FA bias. In 1.5 T and 3.0 T, a SNR of 20 is recommended in ‘high-FA’ regions (approximately FA 0.80) and a SNR of 40 in ‘medium-FA’ regions (approximately

FA 0.45) regions. In ‘low-FA’ regions (approximately FA<0.20) a SNR of 50 is recommended at 1.5 T, and SNR of 70 at 3.0 T<sup>89</sup>.

### ***EPI sequence***

Using a twice-refocused diffusion spin echo pulse results in less eddy current artifacts, albeit a longer TE<sup>76</sup>. The bandwidth is narrow in the phase-encoding direction. Nyquist ghosting artifacts are seen in the phase-encoding direction<sup>91</sup>. Geometric distortion reducing techniques may be considered, e.g. b-zero field mapping, or acquiring and combining k-space in reverse directions<sup>33,72</sup>.

### ***Parallel imaging***

There is a trade-off in the acceleration factor. By collecting fewer lines in k-space SNR decreases, but it also shortens TE, which increases SNR. Using a too high acceleration factor produces noisy images, with noise especially seen in the image center<sup>17,89</sup>. An acceleration factor of 2-2.1 is recommended<sup>17,92</sup>.

### ***Phase-encoding sampling***

Faster sampling in the phase-encoding direction results in less artifacts, except for Nyquist ghosting<sup>75</sup>.

### ***Partial Fourier***

A partial Fourier encoding of 60% is recommended, to shorten TE<sup>17</sup>.

### ***Matrix, Slice thickness***

Matrix and slice thickness will affect SNR. Partial volume effects can be seen in ROI measurements of small structures. Due to averaging, anisotropic voxels will have quantitative measurements that depend on the nerve direction within the voxel<sup>33</sup>.

### ***Fat suppression***

Consider an adiabatic pulse for fat suppression at higher field strengths, since it is more robust to RF inhomogeneities than SPIR<sup>70,120</sup>.

### ***B-zero***

One b-zero (or low b-value) image for every 5-10 diffusion-weighted image is considered optimal<sup>106,107</sup>.

## ***B-value***

Studies examining the median nerve have for fiber tracking found an optimal b-value of 1025 s/mm<sup>2</sup> at 1.5 T<sup>69</sup> and between 1000-1400 s/mm<sup>2</sup> at 3 T<sup>71</sup>. According to Eq. [4] a higher b-value will produce larger echo attenuation, thus a lower SNR<sup>68</sup>. Comparing studies which have used different b-values is problematic, since the trace, MD and FA all depend on the b-value<sup>72,73</sup>.

## ***Diffusion sensitising gradients and directions***

For good tensor orientation estimation, at least 30 diffusion-encoding directions is recommended<sup>15</sup>. As long as the diffusion-encoding gradient directions are well balanced, comparing different gradient schemes between different studies is feasible<sup>74</sup>. Commonly, the b-zero is collected first and thereafter the different diffusion-encoding directions in a series, with all NSA for every direction collected together.

## ***T<sub>R</sub>***

In DTI, a T2-weighted spin echo sequence<sup>14</sup> is used with diffusion-encoding gradient pulses, necessitating a sufficiently long TR. Tissue T1 relaxation time increases with a higher magnetic field and a longer TR is needed<sup>34</sup>.

## ***N<sub>SA</sub>***

To improve SNR, extra NSA or more diffusion-encoding gradient directions can be used, e.g. doubling NSA or gradient directions, will have the same effect on the scanning time<sup>15,74</sup>.  $\text{SNR} \propto \sqrt{\text{NSA}}$ , e.g. four NSA doubles SNR<sup>96</sup>.

## ***Conversion of DICOM***

Converting DICOM to another format, e.g. NIFTI, allows non-vendor-supplied post-processing, e.g. software tools from the FMRIB software library (<http://www.fmrib.ox.ac.uk/fsl>), provided by FSL.

## ***Data quality check***

Check data quality at baseline, following eddy current/motion correction and the final data<sup>148</sup>, e.g. using ‘FSLView’ in three dimensions (FSL). A FA-value > 1 should not be possible. If this is registered (due to negative eigenvalues, since the diffusion-weighted images have higher signal intensity than the b-zero image), it suggests too much noise or non-corrected misregistration<sup>16,148</sup>.

### ***Eddy current correction/Motion correction***

The single-shot diffusion-weighted EPI sequence is relatively insensitive to patient motion during the collection, but motion between acquisitions has to be corrected<sup>15,67</sup>. Large motion can be more difficult to correct, although new techniques are evolving<sup>102,103</sup>. The bipolar diffusion encoding gradients have a high magnitude and long duration, which result in eddy currents that need to be corrected<sup>72</sup>.

### ***B-matrix reorientation***

When adjusting for patient motion, B-matrix should be corrected, i.e. the rotational component should be extracted and applied to the encoding vectors<sup>33,72,101</sup>.

### ***Fitting the diffusion tensor***

There are several ways to estimate the diffusion tensor from the diffusion-weighted data and in FSL ‘ordinary linear least squares methods’ is used<sup>148</sup>.

### ***P parametric map computation***

Finally the parametric maps, e.g. MD and FA, are computed<sup>33,148</sup>.



### 5.3.1 The optimal voxel

The voxel size chosen for analysis will theoretically depend on what type of pathology is of interest to investigate. However, it is optimal to use isotropic voxels, since quantitative measurements thereby are independent of the nerve direction<sup>33</sup>. If an extremely small voxel located within an axon is considered, diffusion is isotropic. When the voxel size is increased, several axons are included and diffusion becomes anisotropic<sup>25</sup>. With further increasing voxel size, additional tissues are included, i.e. collagen, fat, vessels et cetera. As a simple approximation, a 1.0 mm<sup>3</sup> voxel would contain 5100-40000 parallel axons, including other tissues. It would be of interest to investigate the relationship of the voxel size and diffusion data in peripheral nerves. Different voxel sizes might produce equal diffusion data, despite a difference in the contribution of other tissues. Due to the inherently low SNR in DTI, using the largest possible voxel that yield equal diffusion data, would be optimal.

Interestingly, even microcirculation can be analysed with intravoxel incoherent motion imaging DWI<sup>13,149</sup> and functional DWI has been investigated as well<sup>11,31</sup>.

## 5.4 PARKINSON'S DISEASE – SUBSTANTIA NIGRA AND CORPUS CALLOSUM

### Study IV

FA values for SN were close to those previously published<sup>62,116</sup>. The mean  $\lambda_y$  was high in SN, indicating a diffusion direction of SN in an anterior-posterior direction, which can be noted as green in FA-CEI in a study by Vaillancourt<sup>62</sup>*et al.* In a study by Adachi<sup>150</sup>*et al* it was noted that in SN the nerve fibers had a similar direction, indicating that the subROIs were placed correctly in **Study IV**. Locating and delineating subregions within the mesencephalon is difficult with 1.5 T and 3.0 T, although results on 7.0 T are promising<sup>151</sup>. FA was reduced in SN in the PD group, in both DTI series. As in the Vaillancourt<sup>62</sup>*et al* study, MD was not affected, suggesting that FA is a more sensitive biomarker in SN. In the first DTI series, both FA and MD were altered in OB, which could be associated with more advanced synucleinopathy changes, since OB is affected earlier than SN. In PD patients, asymmetry in symptoms<sup>44</sup> and <sup>123</sup>I-Ioflupane putaminal binding is common<sup>152</sup>. However, in **Study IV** the aim was not to study asymmetry in SN diffusion. Since the resolution of the diffusion technique is relatively low and since pars compacta of SN is a small subregion of SN, it would be very difficult to determine asymmetries, and the mean value of both SN was used instead. In a 3.0 T study using anatomical ROI placement significant asymmetric FA values were found in PD patients in the rostral SN<sup>153</sup>, although CV was not evaluated. In a voxel-wise based statistical study on the effect of MR-scanners on brain asymmetry,

changes measured over time on the same scanner were relatively stable. Upgrading of the scanner had a small effect on FA asymmetries, while different scanners significantly affected FA, even when the exact same models of scanners were used<sup>154</sup>. DaTSCAN is a powerful tool in PD diagnostics typically showing reduced <sup>123</sup>I-Ioflupane putaminal binding. However, the radiation dose to the patient must be considered, especially upon repeated examinations.

Diffusion alterations in white matter in PD patients have been observed in the genu of the CC<sup>155</sup>, whereas in another study no alterations were found when the entire CC was examined<sup>63</sup>. In **Study IV**, diffusion was measured in the trunk of the CC and no alterations were observed.

## 5.5 THE ‘HUDDINGE SPINOCEREBELLAR ATAXIA FAMILY’ – BRAIN AND SPINAL CORD

### Study V

Clinical phenotype, ENeG findings and MRI abnormalities of the brain, spinal cord and peripheral nerve of the Swedish ‘Huddinge SCA Family’ are compatible with a slowly progressive autosomal dominant neurodegenerative SCA disorder. Interestingly, this disorder is characterised by atrophy of the cerebellum, brainstem and spinal cord with PNP. Atrophy of the spinal cord has only been described in SCA3/MJD, while it is a rather common finding in Friedreich’s ataxia patients<sup>59,156</sup>. Friedreich’s ataxia and the most common SCAs have been ruled out in the index case and genotype studies are ongoing. Altogether, this disorder is likely to be a rare SCA type.

Conventional MRI is insensitive to detect early brain atrophy and expertise is needed to grade advanced changes in the cerebellum and brainstem. High-resolution 3D MRI volumetry with a voxel size of 1 mm<sup>3</sup> can reliably quantify posterior fossa structures and is better than conventional 2D MRI<sup>157</sup>. MRI volumetry in SCA has shown correlation of specific atrophic regions with clinical symptoms<sup>158</sup>. In **Study V**, T1-weighted imaging with a voxel size of 1 mm<sup>3</sup> was used for MRI volumetry and the brain was segmented into mesencephalon, pons, medulla oblongata, cerebellum and cerebrum<sup>65</sup>. Vermis was not separated from the cerebellar hemispheres, since there are no clear landmarks<sup>159</sup>. All patients in **Study V** had atrophy of the pons, medulla oblongata and cerebellum, which was statistically significant. In SCA the cerebellar dysfunction is mostly caused by Purkinje cell degeneration<sup>160</sup>. The clinical-pathological correlations in spinocerebellar ataxias depend on cerebellar anatomy and its connections to extracerebellar structures, rather than its cortical divisions<sup>57</sup>. In some patients of SCA2, SCA3/MJD, SCA7 and SCA8 the ‘hot cross bun’ sign has been noted<sup>66</sup>, which none of the patients in **Study V** had. Voxel-based morphometry has been used in SCA<sup>65,161,162</sup>. It is a statistical group analysis technique and the small size of

participants in **Study V** precluded this kind of analysis. Due to time-constraints neither DTI nor proton MR spectroscopy of the brain was performed. In SCA1 and SCA2, proton MR spectroscopy has shown decreased concentration of N-acetyl-aspartate in the cerebellum and pons<sup>159</sup>. N-acetyl-aspartate is regarded as a marker of nerve integrity<sup>157</sup>.

**M**RI is a time-consuming examination and it is important for participants to remain motionless during the investigation. Due to time constraints only sagittal T2-weighted images of the spinal cord were performed, although high-resolution 3D sequences would have been preferred. At the midlevel of each vertebra from C1 to Th12, the midsagittal distance of the spinal cord was measured and a mean value was calculated for each individual. In all patients, this mean value was less than for the healthy controls, which was statistically significant. Further studies are necessary to evaluate which specific parts of the spinal cord that are involved. In SCA3/MJD and SCA6 patients, the upper spinal cord has been evaluated with high-resolution T1-weighted MRI and the mean cross sectional area was reduced in SCA3/MJD, but not in SCA6<sup>59</sup>.



## 6. CONCLUSIONS

Nerve diffusion tensor imaging can *in vivo* visualise and analyse peripheral nerves, which have a characteristic diffusion pattern. Due to this pattern, other diffusion imaging approaches can be utilised, such as DDI or unidirectional MIP.

In a clinical study on patients of the Swedish ‘Huddinge SCA Family’, who had clinical and ENeG verified peripheral neuropathy, peripheral nerve diffusion tensor imaging was evaluated. All examined patients had decreased maximum FA in a peripheral nerve, compared to healthy controls, which was statistically significant.

Nerve diffusion tensor imaging can *in vivo* visualise and analyse OBs. Using a novel approach, taking advantage of the DTI technique’s inherent directional information, OBs were localised and analysed in a clinical PD study. In the PD group, compared to healthy controls, mean FA was decreased and MD increased, which was statistically significant. This was hypothesised, since  $\alpha$ -synuclein inclusions and Lewy neurites interfering with nerve structure have been detected in OBs. However, the intra-individual variability was high, owing to the OB’s small size and location susceptible to artifacts, and the difference between the groups was significant only for the first of two series. A major limitation in **Study IV** was the extensive exclusion of participants due to head movements. Several new promising DTI techniques have been developed concerning motion correction<sup>102,103</sup>, artifact reduction<sup>75,97-99</sup> and increased spatial resolution, e.g. parallel RF transmission<sup>147</sup>, a zonally oblique multislice technique to excite a small field of view<sup>145</sup> or even 7.0 T<sup>163</sup>. Using high-field conventional MRI to evaluate OBs in PD patients would be interesting, since 3.0 T and 9.4 T *in vitro* studies of normal OB can identify lamination in OBs<sup>8</sup>, i.e. the cellular layers.

Reporting SNR in future clinical studies could be considered, since DTI is suffering from low SNR, which can lower the precision, accuracy and cause bias in FA.

Pathological nerves have decreased FA, which could be used in a clinical setting. However, implementing nerve diffusion tensor imaging would require a low variance in diffusion measures. Although challenging, nerve diffusion tensor imaging with low variance would be valuable as a non-invasive diagnostic tool in PNP.



## 7. REFERENCES

1. Ropper AH, Brown RH. Adams and Victor's Principles of Neurology, 8th Edition. McGraw-Hill Medical, New York, 2005.
2. Kumar V, Abbas AK, Fausto N. Robbins and Cotran Pathologic Basis of Disease 7th Edition. Elsevier Inc., Philadelphia 2005.
3. Despopoulos A, Silbernagl S. Color Atlas of Physiology, 5th Edition. Thieme 2003.
4. Beaulieu C. The basis of anisotropic water diffusion in the nervous system - a technical review. NMR Biomed. 15(2002)435-455.
5. Maravilla KR. MR Neurography - Imaging Peripheral Nerves. 14th Annual Meeting of ISMRM, Seattle, Washington, USA, 2006.
6. Assaf Y, Blumenfeld-Katzir T, Yovel Y, Basser PJ. AxCaliber: a method for measuring axon diameter distribution from diffusion MRI. Magn Reson Med. 2008 Jun;59(6):1347-54.
7. Duprez TP, Rombaux P. Imaging the olfactory tract (cranial nerve #1). Eur J Radiol 2010 May;74(2):288-98.
8. Burmeister HP, Bitter T, Heiler PM, Irintchev A, Fröber R, Dietzel M, et al. Imaging of lamination patterns of the adult human olfactory bulb and tract: in vitro comparison of standard- and high-resolution 3T MRI, and MR microscopy at 9.4 T. Neuroimage. 2012 Apr 15;60(3):1662-70.
9. Braak H, Bohl JR, Müller CM, Rüb U, de Vos RA, Del Tredici K. Stanley Fahn Lecture 2005: The staging procedure for the inclusion body pathology associated with sporadic Parkinson's disease reconsidered. Mov Disord. 2006 Dec;21(12):2042-51.
10. Greenstein B, Greenstein A. Color Atlas of Neurosciences: Neuroanatomy and Neurophysiology. Thieme 2000.
11. Le Bihan D, Breton E, Lallemand D, Grenier P, Cabanis E, Laval-Jeantet M (1986): MR imaging of intravoxel incoherent motions: Application to diffusion and perfusion in neurologic disorders. Radiology 161:401-407.
12. Chabert S, Scifo P. Diffusion signal in magnetic resonance imaging: origin and interpretation in neurosciences. Biol Res. 2007;40(4):385-400.
13. Koh DM, Collins DJ, Orton MR. Intravoxel incoherent motion in body diffusion-weighted MRI: reality and challenges. AJR Am J Roentgenol. 2011 Jun;196(6):1351-61.
14. Saupe N, White LM, Sussman MS, Kassner A, Tomlinson G, Noseworthy MD. Diffusion tensor magnetic resonance imaging of the human calf: comparison between 1.5 T and 3.0 T – preliminary results. Invest Radiol 2008;43(9):612-618.
15. Mukherjee P, Chung SW, Berman JI, Hess CP, Henry RG. Diffusion Tensor MR Imaging and Fiber Tractography: Technical Considerations. AJNR Am J Neuroradiol 2008 May;29(5):843-52.
16. Tournier JD, Mori S, Leemans A. 2011. Diffusion tensor imaging and beyond. Magn. Reson. Med. 65, 1532-1556.
17. Jaermann T, Pruessmann KP, Valavanis A, Kollias S, Boesiger P. Influence of SENSE on image properties in high-resolution single-shot echo-planar DTI. Magn Reson Med 2006 Feb;55(2):335-42.

18. Mansfield P. Multi-planar image formation using NMR spin echoes. *J. Phys. C: Solid State Phys.*, Vol. 10, 1977.
19. Basser PJ, Mattiello J, Le Bihan D (2005): MR diffusion tensor spectroscopy and imaging. *Biophys J* 66:259-267.
20. Moseley ME, Cohen Y, Kucharczyk J, Mintorovitch J, Asgari HS, Wendland MF, et al. Diffusion-weighted MR imaging of anisotropic water diffusion in cat central nervous system. *Radiology* 1990;176(2):439-45.
21. Moseley ME, Kucharczyk J, Asgari HS, Norman D. Anisotropy in diffusion-weighted MRI. *Magn Reson Med.* 1991 Jun;19(2):321-6.
22. Hajnal JV, Doran M, Hall AS, Collins AG, Oatridge A, Pennock JM, et al. MR imaging of anisotropically restricted diffusion of water in the nervous system: technical, anatomic and pathological considerations. *J Comput Assist Tomogr* 1991;15:1-18.
23. Beaulieu C, Allen PS. Determinants of anisotropic water diffusion in nerves. *Magn Reson Med.* 1994 Apr;31(4):394-400.
24. Beaulieu C, Allen PS. Water diffusion in the giant axon of the squid: Implications for diffusion-weighted MRI of the nervous system. *Magn Reson Med.* 1994 Nov;32(5):579-83.
25. Takahashi M, Hackney DB, Zhang G, Wehrli SL, Wright AC, O'Brien WT, et al. Magnetic resonance microimaging of intraaxonal water diffusion in live excised lamprey spinal cord. *Proc Natl Acad Sci U S A.* 2002 Dec 10;99(25):16192-6.
26. Barazany D, Basser PJ, Assaf Y. In vivo measurement of axon diameter distribution in the corpus callosum of rat brain. *Brain.* 2009 May;132(Pt 5):1210-20.
27. Golabchi FN, Brooks DH, Hoge WS, Mamata H, Maier SE. Comparison of MR Diffusion Anisotropy with Axon Density. In *Proceedings of the 14th Annual Meeting of ISMRM, Seattle, Washington, USA, 2006.*
28. Viera AJ, Garrett JM. Understanding interobserver agreement: the kappa statistic. *Fam Med.* 2005 May;37(5):360-3.
29. Mori S, Crain BJ, Chacko VP, van Zijl PCM. Three-dimensional tracking of axonal projections in the brain by magnetic resonance imaging. *Ann Neurol* 1999;45:265-9.
30. Hasan KM, Walimuni IS, Abid H, Hahn KR. A review of diffusion tensor magnetic resonance imaging computational methods and software tools. *Comput Biol Med.* 2011 Dec;41(12):1062-72.
31. Le Bihan D. Diffusion, confusion and functional MRI. *Neuroimage* 2012 Aug 15;62(2):1131-6.
32. Assaf Y, Kafri M, Shinar H, Chapman J, Korczyn AD, Navon G, et al. Changes in axonal morphology in experimental autoimmune neuritis as studied by high b-value q-space <sup>1</sup>H and <sup>2</sup>H DQF diffusion magnetic resonance spectroscopy. *Magn Reson Med.* 2002 Jul;48(1):71-81.
33. Jones DK. Precision and accuracy in diffusion tensor magnetic resonance imaging. *Top Magn Reson Imaging.* 2010 Apr;21(2):87-99
34. Gold GE, Han E, Stainsby J, Wright G, Brittain J, Beaulieu C. Musculoskeletal MRI at 3.0 T: relaxation times and image contrast. *AJR Am J Roentgenol* 2004;183:343-351.
35. Schmitz BL, Aschoff AJ, Hoffmann MH, Grön G. Advantages and Pitfalls in 3T MR Brain. *AJNR Am J Neuroradiol.* 2005 Oct;26(9):2229-37.



36. Poloni G, Minagar A, Haacke EM, Zivadinov R. Recent developments in imaging of multiple sclerosis. *Neurologist*. 2011 Jul;17(4):185-204.
37. Wolff SD, Balaban RS. Magnetization transfer contrast (MTC) and tissue water proton relaxation in vivo. *Magn Reson Med* 1989;10: 135-144.
38. Schmierer K, Scaravilli F, Altmann DR, Barker GJ, Miller DH. Magnetization transfer ratio and myelin in postmortem multiple sclerosis brain. *Ann Neurol* 2004;56:407-415.
39. Vavasour IM, Laule C, Li DK, Traboulsee AL, MacKay AL. Is the magnetization transfer ratio a marker for myelin in multiple sclerosis? *J Magn Reson Imaging*. 2011 Mar;33(3):713-8.
40. Gambarota G, Mekle R, Mlynárik V, Krueger G. NMR properties of human median nerve at 3 T: proton density, T1, T2, and magnetization transfer. *J Magn Reson Imaging*. 2009 Apr;29(4):982-6.
41. Gambarota G, Krueger G, Theumann N, Mekle R. Magnetic resonance imaging of peripheral nerves: differences in magnetization transfer. *Muscle Nerve*. 2012 Jan;45(1):13-7.
42. Tolosa E, Wenning G, Poewe W. The diagnosis of Parkinson's disease. *Lancet Neurol* 2006;5:75-86.
43. Lees AJ, Hardy J, Revesz T. Parkinson's disease. *Lancet*. 2009 Jun 13;373(9680):2055-66.
44. Stern MB, Lang A, Poewe W. Toward a Redefinition of Parkinson's Disease. *Mov Disord*. 2012 Jan;27(1):54-60.
45. Schapira AH, Tolosa E. Molecular and clinical prodrome of Parkinson disease: implications for treatment. *Nat Rev Neurol*. 2010 Jun;6(6):309-17.
46. Mascalchi M, Vella A, Ceravolo R. Movement disorders: role of imaging in diagnosis. *J Magn Reson Imaging*. 2012 Feb;35(2):239-56.
47. Breen DP, Rowe JB, Barker RA. Role of brain imaging in early parkinsonism. *BMJ*. 2011 Feb 23;342:d638.
48. Morton RJ, Guy MJ, Clauss R, Hinton PJ, Marshall CA, Clarke EA. Comparison of different methods of DatSCAN quantification. *Nucl Med Commun*. 2005 Dec;26(12):1139-46.
49. Scherfler C, Schocke MF, Seppi K, Esterhammer R, Brenneis C, Jaschke W, et al. Voxel-wise analysis of diffusion weighted imaging reveals disruption of the olfactory tract in Parkinson's disease. *Brain* 2006 Feb;129(Pt 2):538-42.
50. Bergmann O, Liebl J, Bernard S, Alkass K, Yeung MS, Steier P, et al. The age of olfactory bulb neurons in humans. *Neuron*. 2012 May 24;74(4):634-9.
51. Doty RL, Shaman P, Dann M. Development of the University of Pennsylvania Smell Identification Test: a standardized microencapsulated test of olfactory function. *Physiol Behav*. 1984 Mar;32(3):489-502.
52. Rombaux P, Duprez T, Hummel T. Olfactory bulb volume in the clinical assessment of olfactory dysfunction. *Rhinology* 2009 Mar;47(1):3-9.
53. Mueller A, Abolmaali ND, Hakini AR, et al. Olfactory bulb volume in patients with idiopathic parkinson's disease – a pilot study. *J Neural Transm* 2005;112:1363-70.
54. Paulson HL. The spinocerebellar ataxias. *J Neuroophthalmol*. 2009 Sep;29(3):227-37.
55. Matilla-Dueñas A. The Ever Expanding Spinocerebellar Ataxias. Editorial. *Cerebellum*. 2012 Mar 24. [Epub ahead of print].

56. Durr A. Autosomal dominant cerebellar ataxias: polyglutamine expansions and beyond. *Lancet Neurol.* 2010 Sep;9(9):885-94.
57. Jacobi H, Hauser TK, Giunti P, Globas C, Bauer P, Schmitz-Hübsch T, et al. Spinocerebellar ataxia types 1, 2, 3 and 6: the clinical spectrum of ataxia and morphometric brainstem and cerebellar findings. *Cerebellum.* 2012 Mar;11(1):155-66.
58. Mandelli ML, De Simone T, Minati L, Bruzzone MG, Mariotti C, Fancellu R, et al. Diffusion tensor imaging of spinocerebellar ataxias types 1 and 2. *AJNR Am J Neuroradiol.* 2007 Nov-Dec;28(10):1996-2000.
59. Lukas C, Hahn HK, Bellenberg B, Hellwig K, Globas C, Schirrig SK, et al. Spinal cord atrophy in spinocerebellar ataxia type 3 and 6: impact on clinical disability. *J Neurol.* 2008 Aug;255(8):1244-9.
60. Schmitz-Hübsch T, du Montcel ST, Baliko L, Berciano J, Boesch S, Depondt C, et al. Scale for the assessment and rating of ataxia: development of a new clinical scale. *Neurology.* 2006 Jun 13;66(11):1717-20.
61. Papademetris X, Jackowski M, Rajeevan N, Constable RT, Staib LH. BioImage Suite: An integrated medical image analysis suite, Section of Bioimaging Sciences, Dept. of Diagnostic Radiology, Yale School of Medicine. <http://www.bioimagesuite.org>.
62. Vaillancourt DE, Spraker MB, Prodoehl J, Abraham I, Corcos DM, et al. High-resolution diffusion tensor imaging in the substantia nigra of de novo Parkinson disease. *Neurology.* 2009 Apr 21;72(16):1378-84.
63. Boelmans K, Bodammer NC, Suchorska B, Kaufmann J, Ebersbach G, Heinze H-J, et al. Diffusion tensor imaging of the corpus callosum differentiates corticobasal syndrome from Parkinson's disease. *Parkinsonism Relat Disord.* 2010 Sep;16(8):498-502.
64. Hofer S, Frahm J. Topography of the human corpus callosum revisited – Comprehensive fiber tractography using diffusion tensor magnetic resonance imaging. *Neuroimage* 2006;32:989-94.
65. Schulz JB, Borkert J, Wolf S, Schmitz-Hübsch T, Rakowicz M, Mariotti C, et al. Visualization, quantification and correlation of brain atrophy with clinical symptoms in spinocerebellar ataxia types 1, 3 and 6. *Neuroimage.* 2010 Jan 1;49(1):158-68.
66. Lee YC, Liu CS, Wu HM, Wang PS, Chang MH, Soong BW. The 'hot cross bun' sign in the patients with spinocerebellar ataxia. *Eur J Neurol.* 2009 Apr;16(4):513-6.
67. Landman BA, Farrell JA, Huang H, Prince JL, Mori S. Diffusion tensor imaging at low SNR: nonmonotonic behaviors of tensor contrasts. *Magn Reson Imaging.* 2008 Jul;26(6):790-800.
68. Bammer R. Basic principles of diffusion-weighted imaging. *Eur J Radiol* 2003;45:169-84.
69. Andreisek G, White LM, Kassner A, Tomlinson G, Sussman MS. Diffusion tensor imaging and fiber tractography of the median nerve at 1.5T: optimization of b value. *Skeletal Radiol* 2009 Jan;38(1):51-9.
70. McRobbie DW, Moore EA, Graves MJ, Prince MR. *MRI from Picture to Proton*, 2nd Edition. Cambridge University Press 2006.
71. Guggenberger R, Eppenberger P, Markovic D, Nanz D, Chhabra A, Pruessmann KP, et al. MR neurography of the median nerve at 3.0 T: Optimization of diffusion tensor imaging and fiber tractography. *Eur J Radiol.* 2012 Jul;81(7):e775-82.
72. Jones DK, Cercignani M. Twenty-five pitfalls in the analysis of diffusion MRI data. *NMR Biomed.* 2010 Aug;23(7):803-20.
73. Hui ES, Cheung MM, Chan KC, Wu EX. B-value dependence of DTI quantitation and sensitivity in detecting neural tissue changes. *Neuroimage.* 2010 Feb 1;49(3):2366-74.

74. Landman BA, Farrell JA, Jones CK, Smith SA, Prince JL, Mori S. Effects of diffusion weighting schemes on the reproducibility of DTI-derived fractional anisotropy, mean diffusivity, and principal eigenvector measurements at 1.5T. *Neuroimage* 2007; 36:1123-1138.
75. Skare S, Newbould RD, Clayton DB, Bammer R. Propeller EPI in the other direction. *Magn Reson Med* 2006;55:1298-1307.
76. Reese TG, Heid O, Weisskoff RM, Wedeen VJ (2003): Reduction of eddy-current-induced distortion in diffusion MRI using a twice-refocused spin echo. *Magn Reson Med* 49:177-182.
77. Pagani E, Hirsch JG, Pouwels PJ, Horsfield MA, Perego E, Gass A, et al. Intercenter differences in diffusion tensor MRI acquisition. *J Magn Reson Imaging*. 2010 Jun;31(6):1458-68.
78. Masutani Y, Aoki S, Abe O, Hayashi N, Otomo K. MR diffusion tensor imaging: recent advance and new techniques for diffusion tensor visualization. *Eur J Radiol* 2003 Apr;46(1):53-66.
79. Seehaus AK, Roebroek A, Chirý O, Kim DS, Ronen I, Bratzke H, et al. Histological Validation of DW-MRI Tractography in Human Postmortem Tissue. *Cereb Cortex*. 2012 Feb 17. [Epub ahead of print].
80. Chung HW, Chou MC, Chen CY. Principles and Limitations of Computational Algorithms in Clinical Diffusion Tensor MR. *AJNR Am J Neuroradiol*. 2011 Jan;32(1):3-13.
81. Huang H, Zhang J, van Zijl PC, Mori S. Analysis of noise effects on DTI-based tractography using the brute-force and multi-ROI approach. *Magn Reson Med*. 2004 Sep;52(3):559-65.
82. Mori S, van Zijl PC. Fiber tracking: principles and strategies – a technical review. *NMR Biomed* 2002; 15:468-480.
83. Guggenberger R, Nanz D, Puipe G, Rufibach K, White LM, Sussman MS, et al. Diffusion tensor imaging of the median nerve: intra-, inter-reader agreement, and agreement between two software packages. *Skeletal Radiol*. 2012 Aug;41(8):971-80.
84. Wang JY, Abdi H, Bakhadirov K, Diaz-Arrastia R, Devous MD Sr. A comprehensive reliability assessment of quantitative diffusion tensor tractography. *Neuroimage*. 2012 Apr 2;60(2):1127-38.
85. Takahara T, Hendrikse J, Kwee TC et al. (2010) Diffusion-weighted MR neurography of the sacral plexus with unidirectional motion probing gradients. *Eur Radiol* 20:1221-6.
86. Takahara T, Kwee TC, Hendrikse J, Van Cauteren M, Koh DM, Niwa T, et al. Subtraction of unidirectionally encoded images for suppression of heavily isotropic objects (SUSHI) for selective visualization of peripheral nerves. *Neuroradiology*. 2011 Feb;53(2):109-16.
87. Takahara T, Imai Y, Yamashita T, Yasuda S, Nasu S, Van Cauteren M. Diffusion weighted whole body imaging with background body signal suppression (DWIBS): technical improvement using free breathing, STIR and high resolution 3D display. *Radiat Med* 2004 Jul-Aug;22(4):275-82.
88. Glockner JF, Hu HH, Stanley DW, Angelos L, King K. Parallel MR imaging: a user's guide. *Radiographics*. 2005 Sep-Oct;25(5):1279-97.
89. Seo Y, Wang ZJ, Morriss MC, Rollins NK. Minimum SNR and acquisition for bias-free estimation of fractional anisotropy in diffusion tensor imaging – a comparison of two analytical techniques and field strengths. *Magn Reson Imaging*. 2012 Oct;30(8):1123-33.
90. Bammer R, Auer M, Keeling SL, Augustin M, Stables LA, Prokesch RW, et al. Diffusion tensor imaging using single-shot SENSE-EPI. *Magn. Reson. Med*. 2002; 48: 128-36.
91. Tsao J. Ultrafast imaging: principles, pitfalls, solutions, and applications. *J Magn Reson Imaging*. 2010 Aug;32(2):252-66.

92. Bhagat YA, Emery DJ, Naik S, Yeo T, Beaulieu C. Comparison of generalized autocalibrating partially parallel acquisitions and modified sensitivity encoding for diffusion tensor imaging. *AJNR Am J Neuroradiol* 2007 Feb;28(2):293-8.
93. Zhou Y, Kumaravel M, Patel VS, Sheikh KA, Narayana PA. Diffusion tensor imaging of forearm nerves in humans. *J Magn Reson Imaging*. 2012 Oct;36(4):920-7.
94. Le Bihan D, Poupon C, Amadon A, Lethimonnier F. Artifacts and pitfalls in diffusion MRI. *J Magn Reson Imaging* 2006 Sep;24(3):478-88.
95. De Panfilis C, Schwarzbauer C. Positive or negative blips? The effect of phase encoding scheme on susceptibility-induced signal losses in EPI. *Neuroimage*. 2005 Mar;25(1):112-21.
96. Brown M, Semelka R. *MRI Basic Principles and Applications*, 3rd Edition. Wiley-Liss 2003.
97. Pipe JG, Farthing VG, Forbes KP. Multishot diffusion-weighted FSE using PROPELLER MRI. *Magn Reson Med* 2002;47:42-52.
98. Holdsworth SJ, Skare S, Newbould RD, Guzmán R, Blevins NH, Bammer R. Readout-segmented EPI for rapid high resolution diffusion imaging at 3 T. *Eur J Radiol*. 2008 Jan;65(1):36-46
99. Iima M, Yamamoto A, Brion V, Okada T, Kanagaki M, Togashi K, et al. Reduced-Distortion Diffusion MRI of the Craniovertebral Junction. *AJNR Am J Neuroradiol*. 2012 Aug;33(7):1321-5.
100. Gallichan D, Scholz J, Bartsch A, Behrens TE, Robson MD, Miller KL. Addressing a systematic vibration artifact in diffusion-weighted MRI. *Hum Brain Mapp*. 2010 Feb;31(2):193-202.
101. Leemans A, Jones DK. The B-matrix must be rotated when correcting for subject motion in DTI data. *Magn Reson Med* 2009 Jun;61(6):1336-49.
102. Aksoy M, Forman C, Straka M, Skare S, Holdsworth S, Hornegger J, et al. Real-time optical motion correction for diffusion tensor imaging. *Magn Reson Med*. 2011 Aug;66(2):366-78.
103. Holdsworth SJ, Aksoy M, Newbould RD, Yeom K, Van AT, Ooi MB, et al. Diffusion tensor imaging (DTI) with retrospective motion correction for large-scale pediatric imaging. *J Magn Reson Imaging*. 2012 Oct;36(4):961-71.
104. Ling J, Merideth F, Caprihan A, Pena A, Teshiba T, Mayer AR. Head injury or head motion? Assessment and quantification of motion artifacts in diffusion tensor imaging studies. *Hum Brain Mapp*. 2012 Jan;33(1):50-62.
105. Roberts TP, Mikulis D. *Neuro MR: principles*. *J Magn Reson Imaging*. 2007 Oct;26(4):823-37.
106. Jones DK, Horsfield MA, Simmons A. Optimal Strategies for Measuring Diffusion in Anisotropic Systems by Magnetic Resonance Imaging. *Magn Reson Med* 1999 Sep;42(3):515-25.
107. Alexander DC, Barker GJ. Optimal imaging parameters for fiber-orientation estimation in diffusion MRI. *Neuroimage*. 2005 Aug 15;27(2):357-67.
108. Andreisek G, White LM, Kassner A, Sussman MS. Evaluation of diffusion tensor imaging and fiber tractography of the median nerve: preliminary results on intrasubject variability and precision of measurements. *AJR Am J Roentgenol* 2010;194(1):W65-W72.
109. Takao H, Hayashi N, Inano S, Ohtomo K. Effect of head size on diffusion tensor imaging. *Neuroimage*. 2011 Aug 1;57(3):958-67.

110. Farrell JA, Landman BA, Jones CK, Smith SA, Prince JL, van Zijl PC, et al. Effects of signal-to-noise ratio on the accuracy and reproducibility of diffusion tensor imaging-derived fractional anisotropy, mean diffusivity, and principal eigenvector measurements at 1.5 T. *J Magn Reson Imaging* 2007 Sep;26(3):756-67.
111. Santarelli X, Garbin G, Ukmar M, Longo R. Dependence of the fractional anisotropy in cervical spine from the number of diffusion gradients, repeated acquisition and voxel size. *Magn Reson Imaging*. 2010 Jan;28(1):70-6.
112. Hodaie M, Quan J, Chen DQ. In vivo visualization of cranial nerve pathways in humans using diffusion-based tractography. *Neurosurgery* 2010 Apr;66(4):788-95.
113. Kabasawa H, Masutani Y, Aoki S, Abe O, Masumoto T, Hayashi N, et al. 3T PROPELLER diffusion tensor fiber tractography: a feasibility study for cranial nerve fiber tracking. *Radiat Med* 2007 Nov;25(9):462-6.
114. Vollmar C, O'Muircheartaigh J, Barker GJ, Symms MR, Thompson P, Kumari V, et al. Identical, but not the same: intra-site and inter-site reproducibility of fractional anisotropy measures on two 3.0 T scanners. *Neuroimage*. 2010 Jul 15;51(4):1384-94.
115. Trip SA, Wheeler-Kingshott C, Jones SJ, Li WY, Barker GJ, Thompson AJ, et al. Optic nerve diffusion tensor imaging in optic neuritis. *Neuroimage*. 2006 Apr 1;30(2):498-505.
116. Rolheiser TM, Fulton HG, Good KP, Fisk JD, McKelvey JR, Scherfler C, et al. Diffusion tensor imaging and olfactory identification testing in early-stage Parkinson's disease. *J Neurol*. 2011 Jul;258(7):1254-60.
117. Unger MM, Belke M, Menzler K, Heverhagen JT, Keil B, Stiasny-Kolster K, et al. Diffusion tensor imaging in idiopathic REM sleep behavior disorder reveals microstructural changes in the brainstem, substantia nigra, olfactory region, and other brain regions. *Sleep*. 2010 Jun;33(6):767-73.
118. Ibarretxe-Bilbao N, Junque C, Marti MJ, Valldeoriola F, Vendrell P, Bargallo N, et al. Olfactory impairment in Parkinson's disease and white matter abnormalities in central olfactory areas: A voxel-based diffusion tensor imaging study. *Mov Disord*. 2010 Sep 15;25(12):1888-94.
119. Morrot G, Bonny JM, Lehallier B, Zanca M. fMRI of human olfaction at the individual level: Interindividual variability. *J Magn Reson Imaging*. 2012 Sep 14. [Epub ahead of print].
120. Schick F. Whole-body MRI at high field: technical limits and clinical potential. *Eur Radiol*. 2005 May;15(5):946-59.
121. Chalian M, Soldatos T, Faridian-Aragh N, Williams EH, Rosson GD, Eng J, et al. 3T Magnetic Resonance Neurography of Tibial Nerve Pathologies. *J Neuroimaging*. 2012 Jan 13. [Epub ahead of print].
122. Lehmann HC, Zhang J, Mori S, Sheikh KA. Diffusion tensor imaging to assess axonal regeneration in peripheral nerves. *Exp Neurol*. 2010 May;223(1):238-44.
123. Takagi T, Nakamura M, Yamada M, Hikishima K, Momoshima S, Fujiyoshi K, et al. Visualization of peripheral nerve degeneration and regeneration: monitoring with diffusion tensor tractography. *Neuroimage*. 2009 Feb 1;44(3):884-92.
124. Della Nave R, Ginestroni A, Tessa C, Salvatore E, De Grandis D, Plasmati R, et al. Brain white matter damage in SCA1 and SCA2. An in vivo study using voxel-based morphometry, histogram analysis of mean diffusivity and tract-based spatial statistics. *Neuroimage*. 2008 Oct 15;43(1):10-9.
125. Kakuda T, Fukuda H, Tanitame K, Takasu M, Date S, Ochi K, et al. Diffusion tensor imaging of peripheral nerve in patients with chronic inflammatory demyelinating polyradiculoneuropathy: a feasibility study. *Neuroradiology*. 2011 Dec;53(12):955-60.

126. Tanitame K, Iwakado Y, Akiyama Y, Ueno H, Ochi K, Otani K, et al. Effect of age on the fractional anisotropy (FA) value of peripheral nerves and clinical significance of the age-corrected FA value for evaluating polyneuropathies. *Neuroradiology*. 2012 Aug;54(8):815-21.
127. Hiltunen J, Suortti T, Arvela S, Seppa M, Joensuu R, Hari R. (2005) Diffusion tensor imaging and tractography of distal peripheral nerves at 3 T. *Clin Neurophysiol* 116:2315-2323.
128. Tagliafico A, Calabrese M, Puntoni M, Pace D, Baio G, Neumaier CE, et al. Brachial plexus MR imaging: accuracy and reproducibility of DTI-derived measurements and fibre tractography at 3.0-T. *Eur Radiol*. 2011 Aug;21(8):1764-71.
129. Guggenberger R, Markovic D, Eppenberger P, Chhabra A, Schiller A, Nanz D, et al. Assessment of Median Nerve with MR Neurography by Using Diffusion-Tensor Imaging - Normative and Pathologic Diffusion. *Radiology*. 2012 Oct;265(1):194-203.
130. Hiltunen J, Kirveskari E, Numminen J, Lindfors N, Göransson H, Hari R. Pre- and post-operative diffusion tensor imaging of the median nerve in carpal tunnel syndrome. *Eur Radiol*. 2012 Jun;22(6):1310-9.
131. Kabakci N, Gurses B, Firat Z, et al. Diffusion tensor imaging and tractography of median nerve: normative diffusion values. *AJR* 2007; 189:923-927.
132. Jambawalikar S, Baum J, Button T, Li H, Geronimo V, Gould ES. Diffusion tensor imaging of peripheral nerves. *Skeletal Radiol* 2010;39(11):1073-1079.
133. Yao L, Gai N. Median nerve cross-sectional area and MRI diffusion characteristics: normative values at the carpal tunnel. *Skeletal Radiol* 2009;38(4):355-361.
134. van der Jagt PK, Dik P, Froeling M, Kwee TC, Nievelstein RA, Ten Haken B, et al. Architectural configuration and microstructural properties of the sacral plexus: A diffusion tensor MRI and fiber tractography study. *Neuroimage*. 2012 Sep;62(3):1792-9.
135. Balbi V, Budzik J, Duhamel A, Bera-Louville A, Le Thuc V, Cotton A. 2011. Tractography of lumbar nerve roots: initial results. *Eur. Radiol*. 21, 1153-1159.
136. Vargas MI, Viallon M, Nguyen D, Delavelle J, Becker M. Diffusion tensor imaging (DTI) and tractography of the brachial plexus: feasibility and initial experience in neoplastic conditions. *Neuroradiology* 2010 Mar;52(3):237-45.
137. Khalil C, Hancart C, Le Thuc V, Chantelot C, Chechin D, Cotten A. Diffusion tensor imaging and tractography of the median nerve in carpal tunnel syndrome: preliminary results. *Eur Radiol* 2008; 18:2283-2291.
138. Stein D, Neufeld A, Pasternak O et al. (2009) Diffusion tensor imaging of the median nerve in healthy and carpal tunnel syndrome subjects. *J Magn Reson Imaging* 29:657-662.
139. Pfefferbaum A, Sullivan EV, Hedehus M, Lim KO, Adalsteinsson E, Moseley M. Agerelated decline in brain white matter anisotropy measured with spatially corrected echo-planar diffusion tensor imaging. *Magn Reson Med* 2000;44(2):259-268.
140. Chhabra A, Chalian M, Soldatos T, Andreisek G, Faridian-Aragh N, Williams E, Belzberg AJ, et al. 3-T high-resolution MR neurography of sciatic neuropathy. *AJR Am J Roentgenol*. 2012 Apr;198(4):W357-64.
141. Adachi Y, Sato N, Okamoto T, Sasaki M, Komaki H, Yamashita F, et al. Brachial and lumbar plexuses in chronic inflammatory demyelinating polyradiculoneuropathy: MRI assessment including apparent diffusion coefficient. *Neuroradiology*. 2011 Jan;53(1):3-11.
142. Budzik JF, Le Thuc V, Demondion X, Morel M, Chechin D, Cotten A. In vivo MR tractography of thigh muscles using diffusion imaging: initial results. *Eur Radiol*. 2007 Dec;17(12):3079-85.

143. Wang CK, Jou IM, Huang HW, Chen PY, Tsai HM, Liu YS, et al. Carpal tunnel syndrome assessed with diffusion tensor imaging. *Eur J Radiol*. 2012 Jan 30. [Epub ahead of print].
144. Meek MF, Stenekes MW, Hoogduin HM, Nicolai JP. In vivo three-dimensional reconstruction of human median nerves by diffusion tensor imaging. *Exp Neurol*. 2006 Apr;198(2):479-82.
145. Wheeler-Kingshott CA, Trip SA, Symms MR, Parker GJ, Barker GJ, Miller DH. In vivo diffusion tensor imaging of the human optic nerve: pilot study in normal controls. *Magn Reson Med*. 2006;56(2):446-51.
146. Morisaki S, Kawai Y, Umeda M, Nishi M, Oda R, Fujiwara H, et al. In vivo assessment of peripheral nerve regeneration by diffusion tensor imaging. *J Magn Reson Imaging*. 2011 Mar;33(3):535-42.
147. Schneider JT, Kalayciyan R, Haas M, Herrmann SR, Ruhm W, Hennig J, et al. Inner-volume imaging in vivo using three-dimensional parallel spatially selective excitation. *Magn Reson Med*. 2012 Jun 21. [Epub ahead of print].
148. Jones DK, Leemans A. 2011. Diffusion tensor imaging. *MethodsMol. Biol.* 711, 127-144.
149. Le Bihan D. 2008. Intravoxel incoherent motion perfusion MR imaging: a wake-up call. *Radiology* 249, 548-552.
150. Adachi M, Hosoya T, Haku T, Yamaguchi K, Kawanami T. Evaluation of the Substantia Nigra in Patients with Parkinsonian Syndrome Accomplished Using Multishot Diffusion-Weighted MR Imaging. *AJNR Am J Neuroradiol*. 1999 Sep;20(8):1500-6.
151. Eapen M, Zald DH, Gatenby JC, Ding Z, Gore JC. Using High-Resolution MR Imaging at 7T to Evaluate the Anatomy of the Midbrain Dopaminergic System. *AJNR Am J Neuroradiol*. 2011 Apr;32(4):688-94.
152. Scherfler C, Seppi K, Donnemiller E, Goebel G, Brenneis C, Virgolini I, et al. Voxel-wise analysis of [<sup>123</sup>I]β-CIT SPECT differentiates the Parkinson variant of multiple system atrophy from idiopathic Parkinson's disease. *Brain*. 2005 Jul;128(Pt 7):1605-12.
153. Prakash BD, Sitoh YY, Tan LC, Au WL. Asymmetrical diffusion tensor imaging indices of the rostral substantia nigra in Parkinson's disease. *Parkinsonism Relat Disord*. [Epub ahead of print]. 2012 Jun 16.
154. Takao H, Hayashi N, Ohtomo K. Effect of scanner in asymmetry studies using diffusion tensor imaging. *Neuroimage* 2011;54(2):1053-62.
155. Gattellaro G, Minati L, Grisoli M, Mariani C, Carella F, Osio M, et al. White matter involvement in idiopathic Parkinson disease: a diffusion tensor imaging study. *AJNR Am J Neuroradiol*. 2009 Jun;30(6):1222-6.
156. Bhidayasiri R, Perlman SL, Pulst SM, Geschwind DH. Late-onset Friedreich ataxia: phenotypic analysis, magnetic resonance imaging findings, and review of the literature. *Arch Neurol*. 2005 Dec;62(12):1865-9.
157. Döhlenger S, Hauser TK, Borkert J, Luft AR, Schulz JB. Magnetic resonance imaging in spinocerebellar ataxias. *Cerebellum*. 2008;7(2):204-14.
158. Mascalchi M. Spinocerebellar ataxias. *Neurol Sci*. 2008 Oct;29 Suppl 3:311-3.
159. Guerrini L, Lolli F, Ginestroni A, Belli G, Della Nave R, Tessa C, et al. Brainstem neurodegeneration correlates with clinical dysfunction in SCA1 but not in SCA2. A quantitative volumetric, diffusion and proton spectroscopy MR study. *Brain*. 2004 Aug;127(Pt 8):1785-95.
160. Edener U, Bernard V, Hellenbroich Y, Gillesen-Kaesbach G, Zühlke C. Two dominantly inherited ataxias linked to chromosome 16q22.1: SCA4 and SCA31 are not allelic. *J Neurol*. 2011 Jul;258(7):1223-7.

161. Ashburner J, Friston KJ. Voxel-based morphometry - The methods. *Neuroimage*. 2000 Jun;11(6 Pt 1):805-21.
162. Goel G, Pal PK, Ravishankar S, Venkatasubramanian G, Jayakumar PN, Krishna N, et al. Gray matter volume deficits in spinocerebellar ataxia: an optimized voxel based morphometric study. *Parkinsonism Relat Disord*. 2011 Aug;17(7):521-7.
163. Polders DL, Leemans A, Hendrikse J, Donahue MJ, Luijten PR, Hoogduin JM. Signal to noise ratio and uncertainty in diffusion tensor imaging at 1.5, 3.0, and 7.0 Tesla. *J Magn Reson Imaging*. 2011 Jun;33(6):1456-63.



## 8. ACKNOWLEDGEMENTS

It all began... at my former colleague Hildur Einarsdottir's dissertation. I got an idea, not an epiphany, on diffusion-weighted imaging, peripheral nerves and neurinomas.

I thank her and I wish to sincerely thank:

Magnus Karlsson, who helped me then and ever since. He is famous for his ability to explain physics to anyone – even me.

Anders Nordell; incredibly friendly and equally smart. Also a good skier, they say.

Mathias Engström, who spins protons and turntables with finesse and ease.

Veli Söderlund; always helpful and very supportive.

Anders Sundin. Without him I wouldn't have registered as a Ph.D. student – and would neither have finished.

Per Svenningsson, a true scientist and an old friend of mine.

Daniel Pettersson and Pierre Vestman whose computer programming has saved me many hours.

Roberto Vargas; always sharing and improving MRI.

Martin Paucar, a curious neurologist. Lennart Blomqvist, a skilful clinician and researcher.

Henry Lindholm, who has an understanding mind and is a good pilot.

All friends and Åsa.

My loving parents.